Article

Cell Chemical Biology

Acyldepsipeptide Analogs Dysregulate Human Mitochondrial ClpP Protease Activity and Cause Apoptotic Cell Death

Graphical Abstract

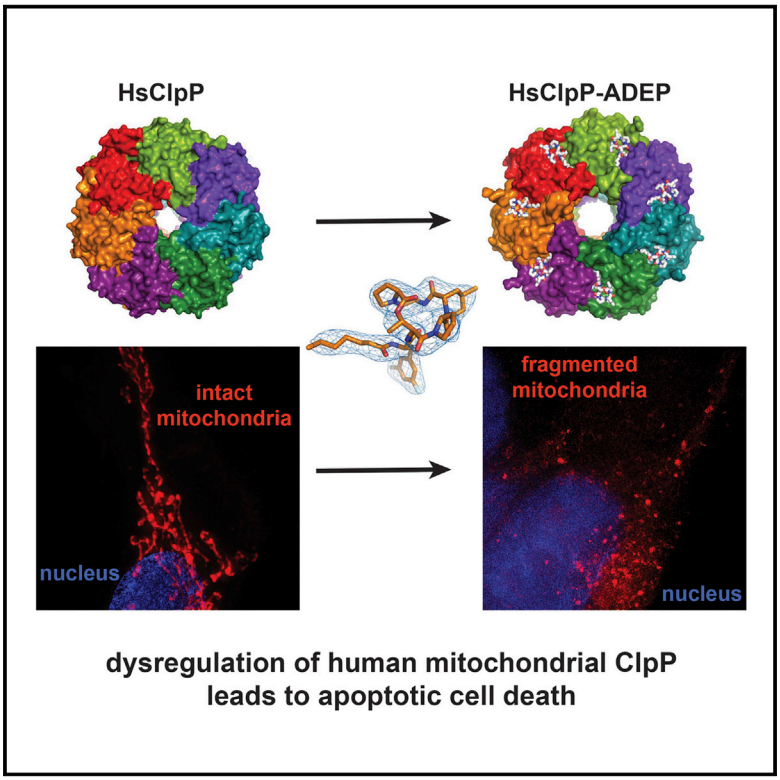

Authors

Keith S. Wong, Mark F. Mabanglo, Thiago V. Seraphim, ..., Robert A. Batey, Aaron D. Schimmer, Walid A. Houry

Correspondence

walid.houry@utoronto.ca

In Brief

Acyldepsipeptides (ADEPs) are potential antibiotics that dysregulate the activity of the highly conserved bacterial ClpP protease. We identified ADEP analogs that are potent dysregulators of the human mitochondrial ClpP (HsClpP). The compounds were found to cause apoptotic cell death. The ADEP-HsClpP co-crystal structure revealed, unexpectedly, HsClpP in the compact conformation.

Highlights

- Acyldepsipeptides dysregulate the activity of human mitochondrial ClpP protease
- Dysregulation of mitochondrial ClpP by ADEPs causes apoptotic cell death
- Co-crystal structure of HsClpP with ADEP reveals another conformation of the protease
- Results suggest a therapeutic potential for ADEPs in cancer treatment

Wong et al., 2018, Cell Chemical Biology *25*, 1017–1030
August 16, 2018
https://doi.org/10.1016/j.chembiol.2018.05.014

CellPress

Cell Chemical Biology
Article

Acyldepsipeptide Analogs Dysregulate Human Mitochondrial ClpP Protease Activity and Cause Apoptotic Cell Death

Keith S. Wong,[1] Mark F. Mabanglo,[1] Thiago V. Seraphim,[1,2] Antonio Mollica,[1,3] Yu-Qian Mao,[1] Kamran Rizzolo,[1] Elisa Leung,[1] Mohamed T. Moutaoufik,[2] Larissa Hoell,[2] Sadhna Phanse,[2] Jordan Goodreid,[4] Leandro R.S. Barbosa,[5] Carlos H.I. Ramos,[6] Mohan Babu,[2] Vito Mennella,[1,3] Robert A. Batey,[4] Aaron D. Schimmer,[7] and Walid A. Houry[1,4,8,*]
[1]Department of Biochemistry, University of Toronto, 661 University Avenue, MaRS Centre, West Tower, Room 1612, Toronto, ON M5G 1M1, Canada
[2]Department of Biochemistry, University of Regina, Regina, SK S4S 0A2, Canada
[3]Cell Biology Program, The Hospital for Sick Children, Toronto, ON M5G 0A4, Canada
[4]Department of Chemistry, University of Toronto, Toronto, ON M5S 3H6, Canada
[5]Institute of Physics, University of São Paulo, São Paulo, São Paulo 05508-090 Brazil
[6]Institute of Chemistry, University of Campinas UNICAMP, Campinas, São Paulo 13083-970 Brazil
[7]Princess Margaret Cancer Centre, University Health Network, Toronto, ON M5G 2M9, Canada
[8]Lead Contact
*Correspondence: walid.houry@utoronto.ca
https://doi.org/10.1016/j.chembiol.2018.05.014

SUMMARY

Acyldepsipeptides (ADEPs) are potential antibiotics that dysregulate the activity of the highly conserved tetradecameric bacterial ClpP protease, leading to bacterial cell death. Here, we identified ADEP analogs that are potent dysregulators of the human mitochondrial ClpP (HsClpP). These ADEPs interact tightly with HsClpP, causing the protease to non-specifically degrade model substrates. Dysregulation of HsClpP activity by ADEP was found to induce cytotoxic effects via activation of the intrinsic, caspase-dependent apoptosis. ADEP-HsClpP co-crystal structure was solved for one of the analogs revealing a highly complementary binding interface formed by two HsClpP neighboring subunits but, unexpectedly, with HsClpP in the compact conformation. Given that HsClpP is highly expressed in multiple cancers and has important roles in cell metastasis, our findings suggest a therapeutic potential for ADEPs in cancer treatment.

INTRODUCTION

Mitochondria in the human cell have multiple important biological functions (Nunnari and Suomalainen, 2012) and require molecular chaperones and proteases to maintain the integrity of their proteome (Fischer et al., 2012). In this regard, the HsClpXP complex, an ATP-dependent protease complex found in the mitochondrial matrix, plays an important role in mitochondrial protein quality control.

HsClpXP is composed of the serine protease HsClpP and the AAA+ ATPase HsClpX. Assembly of the complex involves the capping of the barrel-shaped HsClpP tetradecamer on one or both ends by the HsClpX hexamer (Kang et al., 2002). Protein degradation by ClpXP typically involves the recognition, binding, and unfolding of the substrate by ClpX. The unfolded polypeptide is then threaded through ClpX's central pore into the lumen of ClpP. Once inside, the polypeptide is hydrolyzed by the 14 Ser-His-Asp proteolytic sites of ClpP, and the resultant fragments are expelled from ClpP (Olivares et al., 2016).

The interaction between ClpX and ClpP is partly stabilized by the dynamic docking of IGF loops of ClpX (E436 to G450 in HsClpX; the triplet motif being L439-G440-F441) at specific hydrophobic pockets formed between neighboring ClpP subunits (Amor et al., 2016). Small molecules that abrogate the ClpX-ClpP interaction have been characterized extensively for bacterial ClpXP. Among them, the acyldepsipeptides (ADEPs) (Brötz-Oesterhelt et al., 2005) bind ClpP with high affinity at the same site that normally accommodates the IGF loops of ClpX (Alexopoulos et al., 2012). The high-affinity binding of ADEP also keeps ClpP in a poorly understood activated conformation (Lee et al., 2010; Li et al., 2010). Collectively, these molecular changes allow free access for small peptides, molten globules, and even folded proteins into the lumen of ClpP, causing an increase in degradation activity that is dysregulated, leading to bacterial cell death. Hence, the ADEPs are considered potential antibiotics.

In humans, HsClpP has been shown to physically interact with numerous mitochondrial proteins involved in vital cellular processes such as energy metabolism, mitochondrial translation, mitochondrial protein import, metabolism of amino acids and cofactors, and maintenance of the mitochondrial proteome (Cole et al., 2015; Szczepanowska et al., 2016). HsClpP has also been shown to be important for the survival and metastasis of different types of cancers (Cole et al., 2015; Seo et al., 2016).

Here, we describe the identification of ADEP analogs that target HsClpP. These analogs increase both the peptidase and protease activity of HsClpP *in vitro* and displace HsClpX from HsClpP at low compound concentrations. Treatment of several immortalized cell lines with ADEPs was found to induce cell

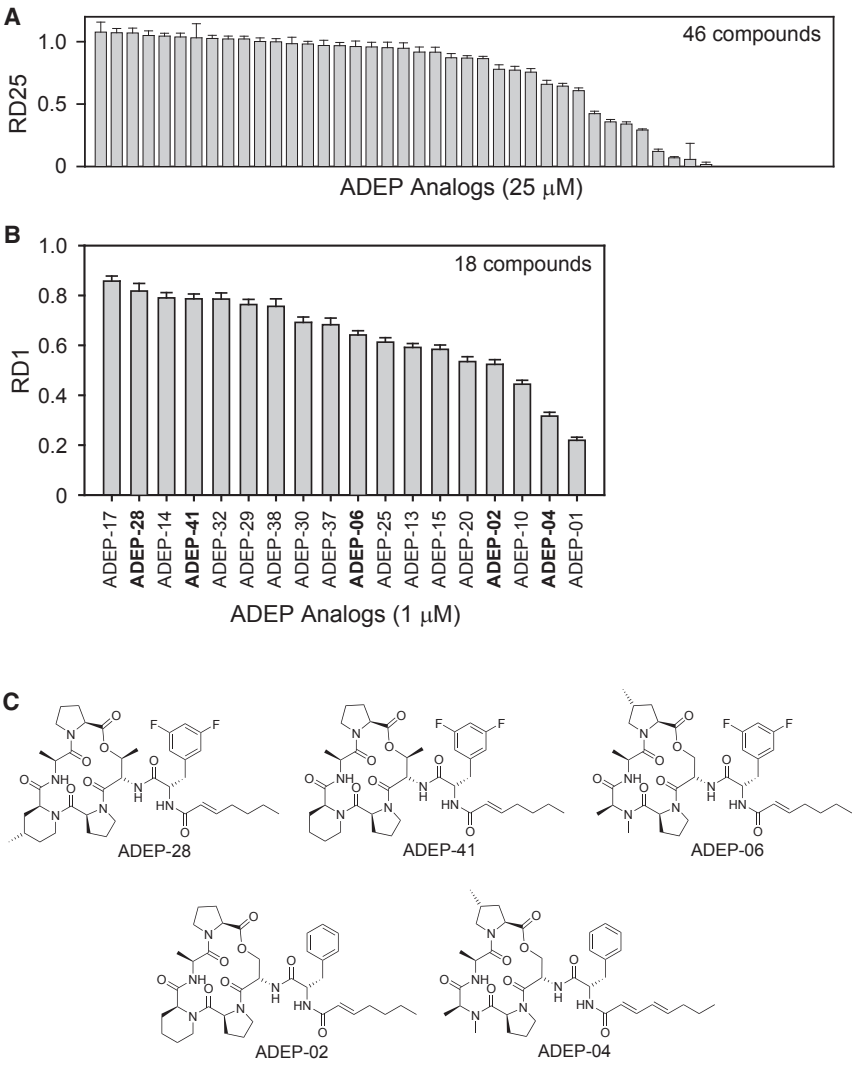

Figure 1. Activity of ADEP Analogs Against HsClpP

(A) RD25 scores of the 46 ADEP analogs tested. SDs are shown as error bars.

(B) RD1 scores of 18 ADEP analogs showing the strongest activation of HsClpP. Names of the five ADEP analogs selected for further experiments are in boldface.

(C) Chemical structures of the five ADEP analogs selected for further experiments.

death in an HsClpP-dependent manner. A cell line deleted of HsClpP showed high tolerance to all ADEP analogs tested. Importantly, ADEP induced cytotoxicity by activating the intrinsic, caspase-dependent apoptosis, leading to cell death. A co-crystal structure of ADEP-HsClpP was obtained and, unexpectedly, revealed an unusual compacted ClpP conformation.

RESULTS

Identification of ADEP Analogs that Dysregulate HsClpP

To identify ADEP analogs that allow HsClpP to degrade folded proteins independent of HsClpX + ATP (i.e., that activate or dysregulate HsClpP), we employed the *in vitro* screening method that we used previously for identifying small-molecule activators of *Escherichia coli* ClpP (EcClpP) (Leung et al., 2011). In this approach, the ability of HsClpP to degrade fluorescein isothiocyanate (FITC)-labeled casein (casein-FITC) was measured and compared with the ability of EcClpAP to degrade casein-FITC. This is quantitatively expressed as the relative degradation (RD) index (Leung et al., 2011) (see Method Details).

Forty-six ADEP analogs (Goodreid et al., 2016) were tested against HsClpP. Initially, the analogs were screened at a final concentration of 25 μM and their RD25 scores (i.e., RD at 25 μM of compound) were measured (Figure 1A). Top hits were then screened at 5 μM and then at 1 μM compound concentration (Figure 1B and Table S1). For follow-up experiments, five ADEP analogs (Figure 1C) were chosen based on their diverse RD1 scores to provide a good representation across the potency spectrum. Furthermore, the selected ADEP analogs have distinct structural differences (Figure 1C).

ADEPs Enhance the Peptidase and Protease Activities of HsClpP

The effects of the ADEPs on the peptidase and protease activities of HsClpP were investigated using *N*-acetyl-Trp-Leu-Ala-AMC (Ac-WLA-AMC) and casein-FITC, respectively. Ac-WLA-AMC was the best peptide substrate for HsClpP among those tested (Figure 2A). The degradation of Ac-WLA-AMC by 6 μM HsClpP (monomeric concentration) has an apparent k_{cat}, K_M, and k_{cat}/K_M lower than that obtained for the degradation of the peptide with 1.5 μM HsClpP in the presence of 4.5 μM HsClpX (compare Figure 2B with Figure S1A, top panel). Similar values were obtained for the degradation of Ac-WLA-AMC using 2 μM EcClpP (Figure S1A, lower panel). In contrast, while there was no detectable degradation of Suc-LY-AMC by HsClpP (Figure 2A), the reported apparent k_{cat} of Suc-LY-AMC degradation by 10 μM EcClpP (protomer concentration) is 2.4 s^{-1} with K_M of 4.4 × 10^3 μM, yielding a k_{cat}/K_M of 5.5 × 10^{-4} s^{-1} μM^{-1} (Bewley et al., 2006). Hence, while HsClpP and EcClpP have similar general peptidase activities against Ac-WLA-AMC, EcClpP seems to have broader substrate preferences compared with HsClpP.

Initial degradation rates data were analyzed using the Hill model. The results for ADEP-28 and ADEP-41 are shown in Figures 2C and 2D, and those for ADEP-06, ADEP-02, and ADEP-04 in Figures S1B and S1C. The kinetic parameters derived are listed in Figure 2E. With all five ADEP analogs, the peptidase activity of HsClpP was similarly enhanced, with V_{max} increased by about 1.8-fold. The Hill coefficients (*h*), ranging from 0.8 for

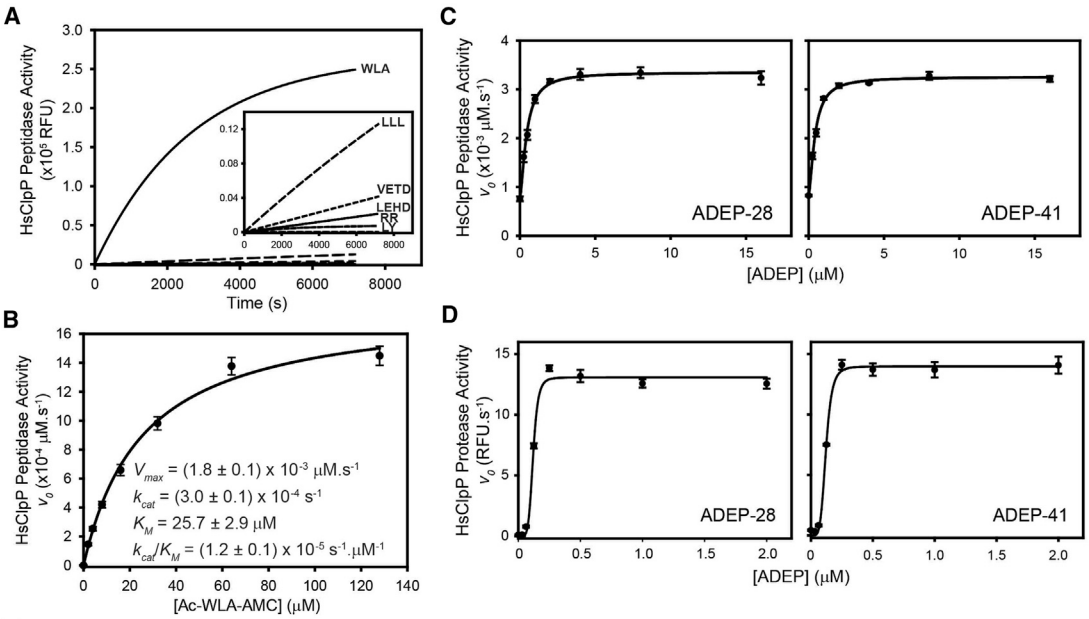

E

	HsClpP Peptidase Activity (Substrate = Ac-WLA-AMC)			HsClpP Protease Activity (Substrate = Casein-FITC)		
	V_{max} (x10^{-3} µM.s^{-1})	h	$K_{0.5}$ (µM)	V_{max} (RFU.s^{-1})	h	$K_{0.5}$ (µM)
ADEP-28	3.4 ± 0.2	1.5 ± 0.2	0.44 ± 0.04	13.1 ± 0.3	6.0 ± 2.8	0.12 ± 0.01
ADEP-41	3.3 ± 0.1	1.5 ± 0.2	0.42 ± 0.03	14.0 ± 0.2	5.0 ± 1.0	0.12 ± 0.01
ADEP-06	2.8 ± 0.2	0.9 ± 0.2	1.8 ± 0.5	10.9 ± 0.4	3.5 ± 0.7	0.9 ± 0.1
ADEP-02	3.2 ± 0.2	0.9 ± 0.2	3.4 ± 0.7	11.3 ± 0.6	3.6 ± 1.1	2.7 ± 0.3
ADEP-04	3.1 ± 0.3	0.8 ± 0.2	4.7 ± 1.6	11.8 ± 0.3	2.6 ± 0.4	9.4 ± 0.6

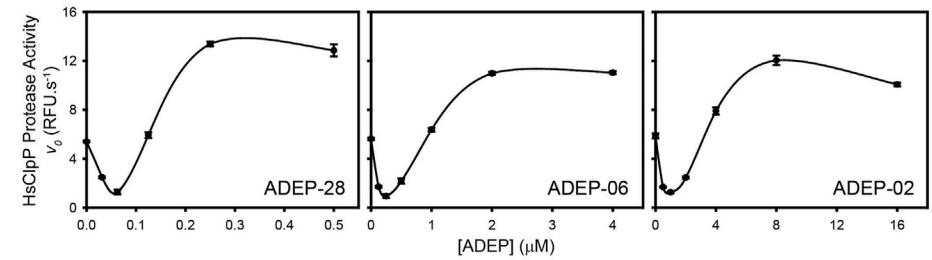

G

	V_{min} Observed (RFU.s^{-1})	[ADEP] at V_{min} (µM)
ADEP-28	1.3 ± 0.2	0.06
ADEP-06	0.9 ± 0.2	0.25
ADEP-02	1.3 ± 0.1	1.00

Figure 2. ADEPs Enhance Both the Peptidase and Protease Activity of HsClpP

(A) Peptidase activity of 8 µM HsClpP (monomeric concentration) against different fluorogenic peptides (at 500 µM final concentration).

(B) Michaelis-Menten kinetics analysis of Ac-WLA-AMC cleavage by 6 µM HsClpP. The kinetic parameters shown were derived from non-linear regression analysis of the initial rates. SDs of the activity data are shown as error bars.

(C) Enhancement of the peptidase activity of 6 µM HsClpP by ADEP-28 (left panel) and ADEP-41 (right panel). Ac-WLA-AMC was used at a final concentration of 100 µM. The kinetic data shown in each panel were derived from three independent replicates. Data for ADEP-06, ADEP-02, and ADEP-04 are shown in Figure S1B.

(D) Enhancement of the protease activity of 3 µM HsClpP by ADEP-28 (left panel) and ADEP-41 (right panel). The kinetic data shown in each panel were derived from three independent replicates. Data for ADEP-06, ADEP-02, and ADEP-04 are shown in Figure S1C.

(E) V_{max}, Hill coefficient (h), and the microscopic apparent dissociation constant ($K_{0.5}$) of all five ADEP analogs tested, derived from the non-linear regression analyses of data collected for the peptidase (left side of table) and protease (right side of table) activity of HsClpP. Errors shown are from curve-fitting.

(F) HsClpP protease activity profiles in the presence of ADEP-28, ADEP-06, and ADEP-02. Solid lines represent simple traces of the kinetic data. SDs are shown as error bars.

(G) Observed minimal rates (mean ± SD) (V_{min} Observed) of casein-FITC degradation and the corresponding ADEP concentration at V_{min} Observed.

ADEP-04 to 1.5 for ADEP-41 (Figure 2E), seem to suggest that the binding of ADEP and the subsequent stimulation of HsClpP's peptidase activity exhibits only marginal positive cooperativity. The apparent dissociation constants ($K_{0.5}$) of the ADEP analogs are closely correlated to their respective RD1 scores. Specifically, the higher the RD1 score of a given analog, the lower is its $K_{0.5}$ (Figure 2E).

Similar to their effects on HsClpP's peptidase activity, all five ADEP analogs activate and enhance the protease activity of HsClpP independently of HsClpX. Notably, the V_{max} measured in the presence of the five ADEP analogs shows little variation (between 10.9 and 14.0 relative fluorescent units [RFU] s^{-1}; Figure 2E). Their $K_{0.5}$, determined by measuring the protease activity of HsClpP, correlates with their respective RD1 scores. Both ADEP-28 and ADEP-41 exhibit the lowest $K_{0.5}$ (0.12 μM), followed by ADEP-06, ADEP-02, and ADEP-04 (Figure 2E). In this assay, unlike in the peptidase activity assay, the binding of ADEP and the subsequent activation and enhancement of HsClpP's protease activity exhibits strong, positive cooperativity. Specifically, enhancement by ADEP-28 has the highest Hill coefficient (Figure 2E).

By comparison, titration of HsClpX and fitting the data to the Hill model yields a V_{max} of 6.88 RFU s^{-1}, a $K_{0.5}$ of 5.7 μM, and mild positive cooperativity (h = 1.25) in HsClpP binding (Figure S1D). These results indicate that the ADEPs exhibit stronger binding to HsClpP than does HsClpX under the conditions of these experiments.

Low Concentration of ADEPs Displaces HsClpX from HsClpXP Complexes

To assess the effects of ADEPs on the interaction between HsClpX and HsClpP, we monitored the degradation of casein-FITC by HsClpXP in the presence of increasing concentrations of ADEP-28, ADEP-06, or ADEP-02. At low ADEP concentrations, the rate of casein-FITC degradation was decreased, down to an observed minimum (V_{min}) that ranges from 0.9 to 1.3 RFU s^{-1} (Figures 2F and 2G). Notably, the ADEP concentration needed to minimize the protease activity is dependent on the apparent binding affinity of each analog. As ADEP concentration was further increased, the protease activity increased likely as the population of ADEP-activated HsClpP increased. Accordingly, the V_{max} achieved with all three ADEP analogs at saturation is identical to the V_{max} previously observed in the absence of HsClpX (Figures 2E and 2F). The initial decrease of protease activity at low ADEP concentrations was not caused by the degradation of HsClpX, HsClpP, or creatine phosphokinase as shown by SDS-PAGE gels (Figures S1E–S1G).

Taken together, the results clearly illustrate that ADEP can induce the dissociation of the HsClpXP complex at low concentrations, resulting in a net loss of protease activity. At higher ADEP concentrations the population of ADEP-activated HsClpP increases, resulting in the restoration and subsequent increase of protease activity.

ADEPs Induce HsClpP-Dependent Cytotoxicity in HEK293 T-REx Cells

To assess the biological impact of ADEPs in targeting HsClpP *in vivo*, we treated HEK293 T-REx wild-type (WT) and *CLPP*$^{-/-}$ cells with serially diluted ADEP-28, ADEP-41, ADEP-06, ADEP-02, and ADEP-04, followed by an assessment of their survival 72 hr post treatment. For WT cells, all five ADEP analogs were found to be cytotoxic with IC_{50} values between 0.36 and 8.20 μM (Figures 3A, 3B, and S2A). In comparison, IC_{50} of cisplatin on HEK293 cells has been reported at 0.43 μM and that of the dihydrofolate reductase-targeting metoprine at 0.80 μM (Bram et al., 2006).

Importantly, the cytotoxicity of ADEPs showed a strong, linear correlation with their respective apparent binding affinity for HsClpP (Figure 3C), revealing a direct link between the potency of ADEPs in activating HsClpP and their cytotoxicity. Furthermore, ADEP-induced cytotoxicity is HsClpP-dependent, as *CLPP*$^{-/-}$ cells, which lack endogenous HsClpP, are highly resistant to all five ADEP analogs (Figures 3A, 3B, and S2A). Hence, these ADEPs are likely acting on-target in cells, although interactions with other proteins that do not cause cytotoxicity cannot yet be ruled out.

It should be noted that, using deep proteomics profiling of mitochondrial extracts isolated from WT and *CLPP*$^{-/-}$ HEK293 T-REx cells, 281 distinct mitochondrial proteins were identified covering 24% of the estimated human mitochondrial proteome (281 of 1,158 human mitochondrial proteins from MitoCarta2.0 inventory [Calvo et al., 2016]). Of these, only 19 mitochondrial proteins in *CLPP*$^{-/-}$ were significantly ($p \leq 0.05$) altered with more than 1.5-fold change compared with WT cells (Table S2). This indicates that there are no drastic changes in the mitochondrial proteome upon *CLPP* deletion under the conditions tested.

Cellular Sensitivity to ADEP Correlates with Intracellular HsClpP Expression Levels

Given that ADEP-induced cytotoxicity depends on HsClpP, the effect of intracellular HsClpP levels on the cell's sensitivity to ADEP was examined. HsClpP overexpression was achieved using HEK293 T-REx overexpressing a C-terminally FLAG-tagged, full-length HsClpP (CLPP-FLAG) upon induction with doxycycline (Dox). Similarly, HEK293 T-REx + $CLPP_{S153A}$-FLAG overexpresses a C-terminally FLAG-tagged, full-length inactive HsClpP(S153A) mutant.

HsClpP overexpression was confirmed by western blot analysis. As shown in Figure 3D, high expression of FLAG-tagged HsClpP or FLAG-tagged $HsClpP_{S153A}$ was detected in HEK293 T-REx + CLPP-FLAG and HEK293 T-REx + $CLPP_{S153A}$-FLAG, respectively, in the presence of Dox (band I). Due to leakiness of the Dox-inducible promoter, expression of the FLAG-tagged HsClpP proteins (WT or S153A mutant) was also detected in the absence of Dox, albeit at significantly lower levels (band I). Expression of endogenous HsClpP was also observed (band III). Interestingly, an additional HsClpP band (band II) that corresponds to a slightly larger HsClpP protein but lacks the C-terminal FLAG tag (α-FLAG panel) was observed in both HEK293 T-REx + CLPP-FLAG (with or without Dox) and HEK293 T-REx + $CLPP_{S153A}$-FLAG (with Dox only) cells. Band II is likely the result of the C-terminal FLAG tag being cleaved via HsClpP's own proteolytic activity.

To determine the effect of intracellular HsClpP expression on the cell's sensitivity to ADEP, we grew HEK293 T-REx WT, *CLPP*$^{-/-}$, HEK293 T-REx + CLPP-FLAG, and HEK293 T-REx + $CLPP_{S153A}$-FLAG cells in the presence of ADEP-41 with or without Dox. Without Dox, both HEK293 T-REx + CLPP-FLAG

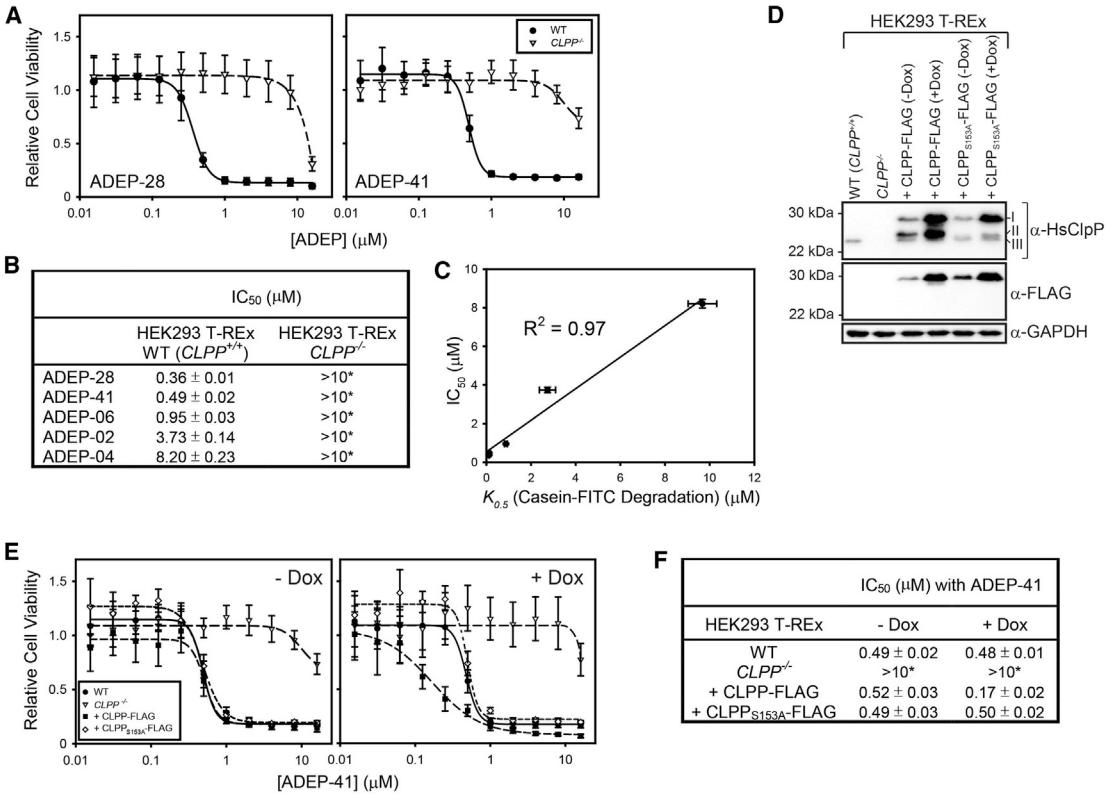

Figure 3. ADEP Induces HsClpP-Dependent Cytotoxicity in HEK293 T-REx Cells

(A) Cytotoxicity profiles of HEK293 T-REx WT (*CLPP*$^{+/+}$) and HEK293 T-REx *CLPP*$^{-/-}$ cells treated with ADEP-28 (left panel) and ADEP-41 (right panel). Relative cell viability ± SDs (shown as error bars) was calculated by normalizing data collected from four independent replicates to the DMSO-only control. Data for ADEP-06, ADEP-02, and ADEP-04 are shown in Figure S2A.

(B) Quantification of the cytotoxicity data collected for the five ADEP analogs tested. For WT, IC_{50} values ± curve-fitting errors were derived from non-linear regression analysis using a standard dose-response equation (see STAR Methods). For *CLPP*$^{-/-}$, the lack of a minimum plateau in the cytotoxicity profiles prohibited non-linear regression analysis. Instead, IC_{50} values were estimated and are expressed in numerical ranges (denoted by asterisks).

(C) IC_{50} values of the five ADEP analogs tested strongly correlate with their respective apparent binding affinity ($K_{0.5}$) to HsClpP *in vitro* (shown in Figure 2E) that were derived from the protease activity data.

(D) Western blots on whole cell lysates of HEK293 T-REx WT, *CLPP*$^{-/-}$, HEK293 T-REx + CLPP-FLAG, and HEK293 T-REx + $CLPP_{S153A}$-FLAG. The absence or presence of Dox in the tissue culture is indicated as "−Dox" or "+Dox", respectively. The primary antibody used in each blot is indicated to the right of each panel. Protein molecular weight markers are shown on the left. For the α-HsClpP blot, band I corresponds to HsClpP (WT or S153A mutant)-FLAG, band II corresponds to HsClpP (WT or S153A mutant) that is missing the C-terminal FLAG tag, and band III corresponds to endogenous HsClpP.

(E) ADEP-41 cytotoxicity profiles of HEK293 T-REx WT, *CLPP*$^{-/-}$, and WT cells that overexpress the C-terminal FLAG-tagged HsClpP (+CLPP-FLAG) or the proteolytically inactive mutant (+$CLPP_{S153A}$-FLAG). Data collected on cells grown without Dox are shown on the left panel; data collected in the presence of 0.4 μg/mL Dox are shown on the right panel.

(F) IC_{50} values derived from the cytotoxicity profiles of (E). For HEK293 T-REx *CLPP*$^{-/-}$, IC_{50} were estimated and are expressed in numerical ranges (denoted by asterisks).

and HEK293 T-REx + $CLPP_{S153A}$-FLAG were equally sensitive to ADEP-41 as WT, while *CLPP*$^{-/-}$ was resistant (Figure 3E, −Dox panel). Accordingly, the IC_{50} for WT, HEK293 T-REx + CLPP-FLAG, and HEK293 T-REx + $CLPP_{S153A}$-FLAG were similar within statistical errors (Figure 3F). In the presence of Dox, the increase in intracellular HsClpP level rendered HEK293 T-REx + CLPP-FLAG highly sensitive to ADEP-41 compared with WT (Figure 3E, +Dox panel), resulting in a significant decrease in IC_{50} (Figure 3F). Importantly, HEK293 T-REx + $CLPP_{S153A}$-FLAG, which expresses native HsClpP at the WT level but can only overexpress the proteolytically inactive HsClpP mutant, maintains WT-like sensitivity to ADEP-41 (Figure 3E, +Dox panel) and shows no change in IC_{50} (Figure 3F). These results clearly illustrate that the intracellular expression level of proteolytically active HsClpP can modulate the cell's sensitivity to ADEP, with higher expression resulting in greater sensitivity.

Aside from HEK293 T-REx, the cellular sensitivity to ADEP-41 was investigated in several other commonly used cell lines. These include HeLa (regular), HeLa T-REx, U2OS, and undifferentiated SH-SY5Y (Figures S2B and S2C). The IC_{50} for all cell lines were similar, with undifferentiated SH-SY5Y having a slightly higher value (Figure S2C). However, U2OS and undifferentiated SH-SY5Y have lower levels of HsClpP than the other cell lines (about 20% and 40% relative to HEK293 T-REx, respectively) (Figure S2D). Hence, in addition to the intracellular level of HsClpP, ADEP sensitivity varies slightly by cell type.

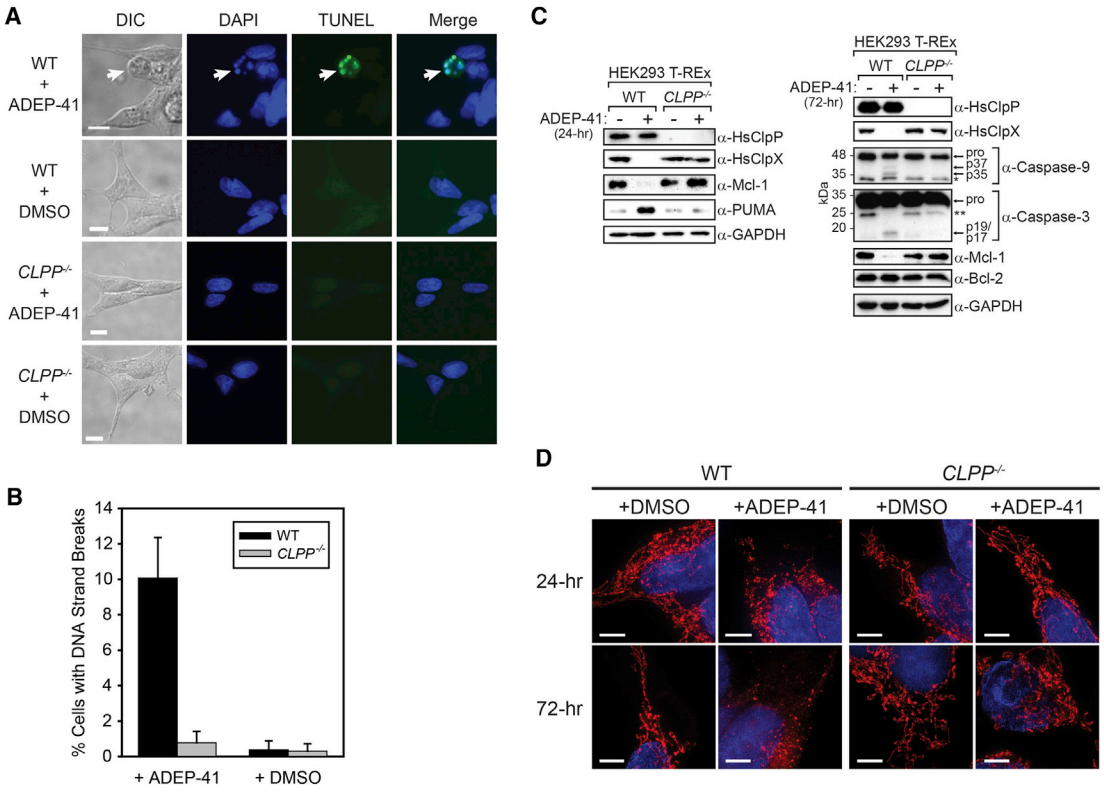

Figure 4. ADEP Induces Intrinsic, Caspase-Dependent Apoptosis

(A) Light (differential interference contrast [DIC]) and fluorescence (DAPI, TUNEL) microscopy images of HEK293 T-REx WT and HEK293 T-REx *CLPP*$^{-/-}$ treated with 10 μM ADEP-41 or DMSO for 72 hr. The DAPI + TUNEL (Merge) images are shown on the far-right panels. WT cells showing fragmentation of chromosomal DNA and presence of DNA strand breaks (i.e., TUNEL-positive) are marked with white arrows. The scale bars in the DIC panels represent a length of 50 μm.

(B) Quantification of WT and *CLPP*$^{-/-}$ cells treated with ADEP-41 or DMSO that have acquired DNA strand breaks as observed in the TUNEL assay. SDs of three independent replicates are shown as error bars.

(C) Western blots for HsClpP, HsClpX, and major marker proteins for caspase-dependent apoptosis, on whole-cell lysates of WT and *CLPP*$^{-/-}$ cells treated with 20 μM ADEP-41 for 24 hr (left panels) or 10 μM ADEP-41 for 72 hr (right panels). "pro" denotes the proform of the caspases. Single asterisk denotes a cross-reacting protein band with the α-caspase-9 antibody; double asterisk denotes a possibly non-activated intermediate of caspase-3 processing. GAPDH was used as a loading control. The primary antibodies used in each blot are indicated to the right of each panel. Protein molecular weight markers are shown on the left.

(D) 3DSIM analysis of mitochondrial morphology in WT and *CLPP*$^{-/-}$ cells during apoptosis. Cells were treated with 2 μM ADEP-41 or DMSO for 24 or 72 hr prior to imaging. Mitochondria were stained with MitoTracker Red CMXRos and are shown in red. Nuclei were stained with Hoechst 33342 and are shown in blue. Representative images of at least three independent replicates are shown. Scale bars correspond to a length of 5 μm.

ADEP Activates the Intrinsic, Caspase-Dependent Apoptosis in HEK293 T-REx Cells

The cellular mechanism underlying ADEP's cytotoxicity on HEK293 T-REx cells was further investigated. First, morphological changes of WT and *CLPP*$^{-/-}$ exposed to ADEP-41 for 72 hr were examined by microscopy. ADEP-41-treated WT cells appeared compact and spherical, and exhibited a significant loss of adherence to the growth surface (Figures 4A and S3A). This is in stark contrast to DMSO-treated WT cells as well as to *CLPP*$^{-/-}$ cells that are resistant to ADEP-induced cytotoxicity (Figures 4A and S3A). Furthermore, blebs were observed on the surface of affected WT cells (indicated by white arrows in Figure 4A).

Both cell shrinkage and surface bleb formation are strong indicators of apoptosis (Elmore, 2007). Apoptosis in WT cells induced by ADEP-41 was confirmed by TUNEL assay, indicating the fragmentation of chromosomal DNA that congregate into small, condensed bodies (appearing as multiple foci) upon compound treatment (Figure 4A). In contrast, DMSO-treated WT cells have intact chromosomal DNA and were not TUNEL labeled. Importantly, both ADEP-treated and DMSO-treated *CLPP*$^{-/-}$ cells have normal nuclei and intact chromosomal DNA (Figure 4A). Quantification of cells with positive TUNEL labeling revealed that about 20 times more of the ADEP-41-treated WT cells were TUNEL-positive compared with DMSO-treated ones, or compared with *CLPP*$^{-/-}$ cells treated with ADEP-41 or DMSO (Figure 4B).

Subsequently, the intracellular expression of signature apoptotic protein markers was examined by western blotting. The expression of both HsClpP and HsClpX was also examined. Treatment with ADEP for 24 or 72 hr did not change HsClpP levels in WT cells compared with DMSO (Figure 4C). In contrast, HsClpX was no longer detected in WT cells treated with ADEP-41 for either duration (Figure 4C), despite the fact that HsClpX is not degraded by the ADEP-activated HsClpP *in vitro* (Figures S1E–S1G). To determine whether the loss of HsClpX

has any potential role in ADEP-induced apoptosis, a *CLPX* gene disruption was obtained using CRISPR/Cas9, which reduces HsClpX expression by ≥97% (Δ*CLPX**; Figure S3B). Significant reduction of HsClpX levels had no statistically significant impact on the cells' sensitivity to ADEP-28 regardless of HsClpP expression (Figure S3C). Hence, the loss of HsClpX in ADEP-treated WT cells may be part of a stress response mechanism. Alternatively, HsClpX could be degraded by other mitochondrial proteases.

After 24 hr of ADEP-41 treatment, no activation-specific cleavage was observed for caspase-8, caspase-9, or caspase-3 (data not shown). However, the anti-apoptotic Mcl-1 protein was degraded in WT cells but not in *CLPP*$^{-/-}$ cells (Figure 4C). Conversely, the pro-apoptotic PUMA protein was significantly upregulated in WT cells in contrast to *CLPP*$^{-/-}$ cells (Figure 4C). These changes in the intracellular levels of Mcl-1 and PUMA are strong indications for the initiation of the intrinsic apoptotic pathway.

After 72 hr of ADEP-41 treatment, the degradation of Mcl-1 in WT cells remained clearly observable (Figure 4C). Notably, there was no change in the level of anti-apoptotic Bcl-2 protein, suggesting that the loss of Mcl-1 is a specific cellular response to the ADEP-41 treatment. Importantly, activation-specific cleavage was detected for both caspase-9 and caspase-3, which produced the characteristic p37 and p35 fragments for caspase-9, and p19/p17 for caspase-3 (Figure 4C). Furthermore, no activation-specific cleavage was observed for caspase-8 (Figure S3D). Given that caspase-9 is functionally associated with the intrinsic apoptotic pathway while caspase-8 is linked to the extrinsic pathway (McIlwain et al., 2013), we conclude that treatment of WT cells with ADEP activates the intrinsic apoptotic pathway, leading to cell death.

ADEP Induces Mitochondrial Fragmentation and Abolishes OXPHOS in HEK293 T-REx Cells

Given that mitochondrial fragmentation and outer membrane permeabilization (MOMP) are hallmarks of apoptosis (Landes and Martinou, 2011), the impact of ADEP on mitochondrial morphology and oxidative phosphorylation (OXPHOS) was further investigated. Mitochondria in HEK293 T-REx WT and *CLPP*$^{-/-}$ treated with ADEP-41 or DMSO for 24 and 72 hr were examined below the diffraction limit by super-resolution 3D structured illumination microscopy (3DSIM). As shown in Figure 4D, WT cells treated with ADEP-41 already showed clear signs of mitochondrial fragmentation after 24 hr compared with DMSO-treated cells. Furthermore, the fragmentation observed was very significant after 72 hr of treatment. In contrast, *CLPP*$^{-/-}$ cells treated with ADEP-41 showed no change in mitochondrial morphology for either duration.

MOMP is known to dissipate the mitochondrial electrochemical gradient ($\Delta\psi$) during apoptosis (Kroemer and Reed, 2000), which abolishes OXPHOS. As such, OXPHOS in WT and *CLPP*$^{-/-}$ cells treated with ADEP-28 or DMSO for 24 hr was examined using the Seahorse extracellular flux (XF) analyzer. Notably, OXPHOS in ADEP-28-treated WT cells was largely abolished, as exemplified by the large reduction in oxygen consumption rate associated with basal respiration (~86%) and ATP synthase activity (~91%), relative to DMSO-treated WT cells (Figures S3E and S3F, upper panel). Furthermore, ADEP-treated WT cells showed a higher basal extracellular acidification rate that was largely unresponsive to ATP synthase inhibition (Figure S3F, lower panel), suggesting the cell's reliance on glycolysis for energy metabolism as a result of losing OXPHOS. Both events can be explained by $\Delta\psi$ dissipation as a result of MOMP.

The fragmentation of mitochondria and loss of OXPHOS from $\Delta\psi$ dissipation both provide confirmative evidence that ADEP induces apoptosis in HsClpP-expressing cells.

ADEP Binding Induces Conformational Changes in the HsClpP Tetradecamer

To further understand the mechanism by which ADEP binding leads to HsClpP dysregulation, we determined the structure of HsClpP co-crystallized with ADEP-28 (Figure 5A) at 2.8-Å resolution (Table S3). ADEP-28 has high binding affinity for HsClpP (Figure 2E). In the crystal, the asymmetric unit contains a single heptameric ring that forms the HsClpP tetradecamer with a second ring related to the first by crystallographic symmetry (Figures 5A–5E and Table S3). Of the 277 residues in HsClpP, no electron density was observed for residues 252–277 (chains A–D) or 251–277 (chains E–G) at the C terminus, whereas residues 1–57 that contain the mitochondrial transport signal were omitted during cloning (Figure 5B). We also observed extra electron density attached to the thiol group of Cys86 in each subunit, indicating covalent modification (Figure 5F). Mass spectrometry analysis identified this modification as potentially being persulfidation of the cysteine thiol (data not shown).

As observed for other ClpPs, ADEP-28 bound to the hydrophobic pocket formed by two neighboring HsClpP subunits (Figure 5A). Clear electron densities for all seven ADEP-28 molecules per heptameric ring were observed (Figure 5C). The N-terminal axial loops were ordered (Figures 5A, 5D, and 5E), as observed previously in the ADEP-bound EcClpP (Li et al., 2010), *Neisseria meningitidis* ClpP (NmClpP) (Goodreid et al., 2016), and *Mycobacterium tuberculosis* ClpP (MtClpP) (Schmitz et al., 2014). ADEP-28 binding enlarged the HsClpP's axial pore (Figure 5A). Interestingly, ADEP-28-HsClpP adopts a compact conformation (Figure 5A), which has not been seen in other ADEP-bound ClpP structures characterized to date (Goodreid et al., 2016; Lee et al., 2010; Li et al., 2010; Schmitz et al., 2014) (and PDB: 5VZ2). We will first describe the ADEP-binding pocket and then discuss the distal molecular rearrangements observed.

The binding of ADEP-28 to HsClpP induces local structural changes at and around the binding pocket between two neighboring subunits, forming a highly complementary surface for the ADEP molecule (Figures 6A and S4). Normally, the N-terminal β1-β0 hairpins forming the axial loops are disordered in the absence of ADEP (Figure 5A). An ionic interaction between R78 of one subunit and E109 of the neighboring subunit secures the interface between the subunits (Figure 6Ai). Upon ADEP-28 binding, ordered axial loop formation places E64 between R78 of the same subunit and E109 of the neighboring subunit, creating three new hydrogen bonds (H bonds) that also involve R78 interacting with the intra-subunit E82 (Figure 6Aii). These interactions stabilize a widened surface with the bound ADEP-28 acting as a wedge.

At the ADEP-28/ClpP interface, two Tyr residues, Y118 of one subunit and Y138 of the neighboring subunit, form H bonds with carbonyl carbon atoms of the depsipeptide ring (Figures 6Aii and

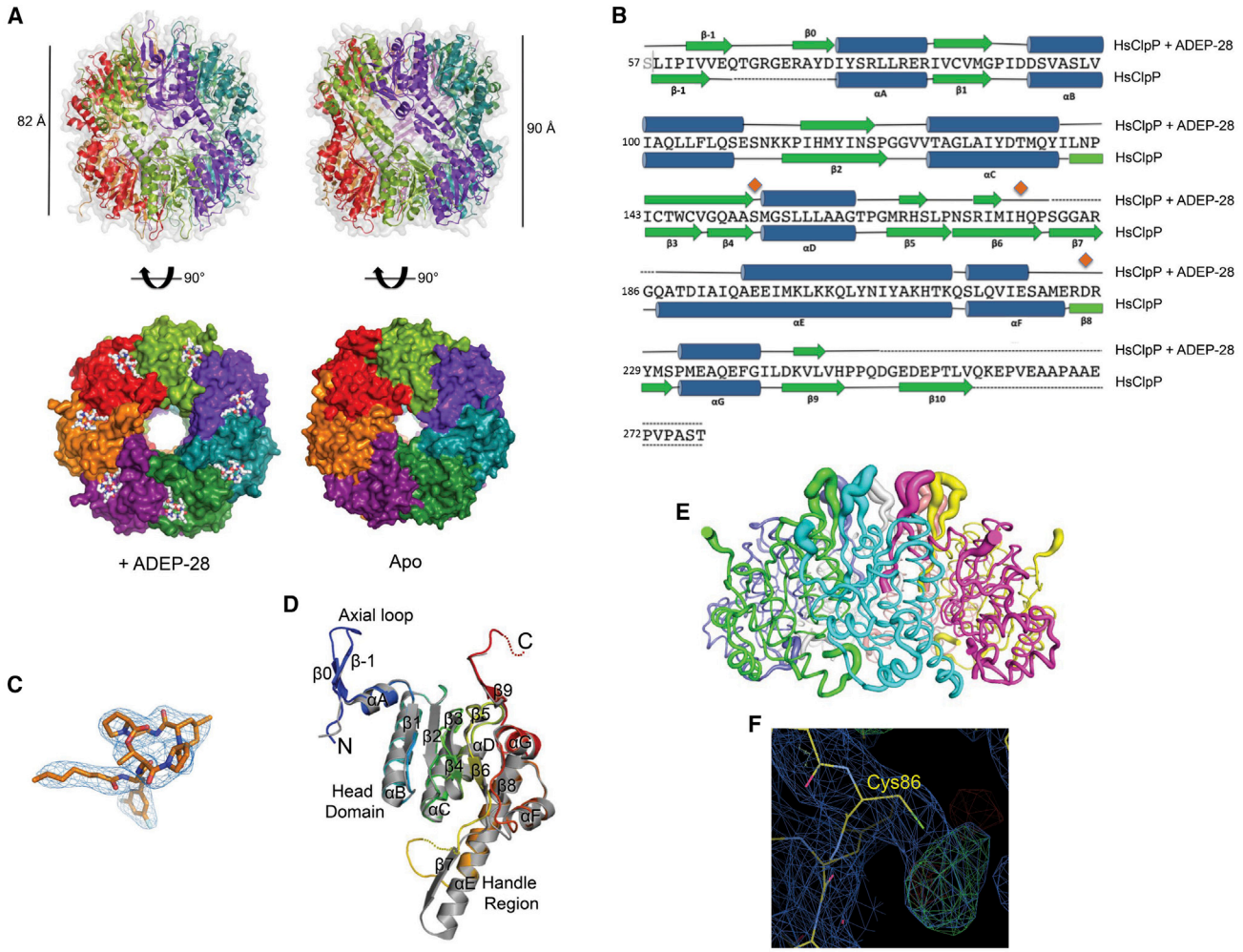

Figure 5. ADEP-Binding Induces Conformational Changes in the HsClpP Tetradecamer

(A) The ADEP-28-bound (left) and apo form (right) of the HsClpP tetradecamer, shown in side views (top) and top views (bottom). The bound ADEP-28 are shown as sticks. The distances shown were measured between the Cα atoms of E109 (helix αB) located on the surface of two apposing ClpP rings.

(B) The sequence and the secondary structure of HsClpP in the presence and absence of ADEP-28. The catalytic triad residues (S153, H178, and D227) are indicated with orange diamonds. Note that Ser57 was introduced due to cloning.

(C) $2F_o$-F_c electron density map of ADEP-28 contoured at 1.0σ.

(D) Superposition of the monomeric structures of ADEP-28-bound HsClpP (chain A; rainbow-colored from N terminus to C terminus) and apo HsClpP (in gray; PDB: 1TG6, chain A), viewed from within the HsClpP lumen.

(E) Cartoon putty representation of a single ring of ADEP-28-HsClpP complex with thicker tubes indicating higher *B* factors.

(F) $2F_o$-F_c map (blue mesh) contoured at 1.0σ, and F_o-F_c map (green mesh) contoured at 3.5σ showing covalent modification on the thiol group of Cys86 that is observed in each HsClpP subunit.

S4A). Similar interactions have been reported for other bacterial ClpP-ADEP complexes (Goodreid et al., 2016; Li et al., 2010; Schmitz et al., 2014). In addition, an H_2O-mediated H bond is observed between Q107 and the amide carbonyl connecting the hydrophobic tail and 3,5-difluorophenyl moieties of ADEP-28. A Trp residue (W146) in HsClpP forms a hydrophobic stacking interaction with the 3,5-difluorophenyl moiety of ADEP-28 (Figures 6Aii and S4A). The corresponding residues in bacterial ClpPs all have smaller aliphatic side chains, which yield a smaller hydrophobic surface for the difluorophenyl group (Figure S4B).

The depsipeptide ring is solvent exposed but with its nitrogenous, heterocyclic rings forming stacking interactions with the aromatic or hydrophobic residues in the ADEP-binding pocket. In particular, the methyl piperidine ring of ADEP-28 (Figure 6Aii on far right of ADEP-28 when viewed as shown) sits directly on top of H168 of β5. The relatively small side chain of the His residue is likely to provide additional space to accommodate the methyl piperidine ring and in turn strengthens the ADEP-28-HsClpP interaction, resulting in the high apparent binding affinity observed (Figure 2E). In contrast, the equivalent residue in bacterial ClpPs is either Tyr, Phe, or Met, all of which are bulkier than the His residue of HsClpP (Figure S4B).

As mentioned above, binding of ADEP-28 induces the formation of the N-terminal β1-β0 hairpins (residues 58–74), creating ordered axial loops (Figures 5A, 5D, and 5E). While the β1 and

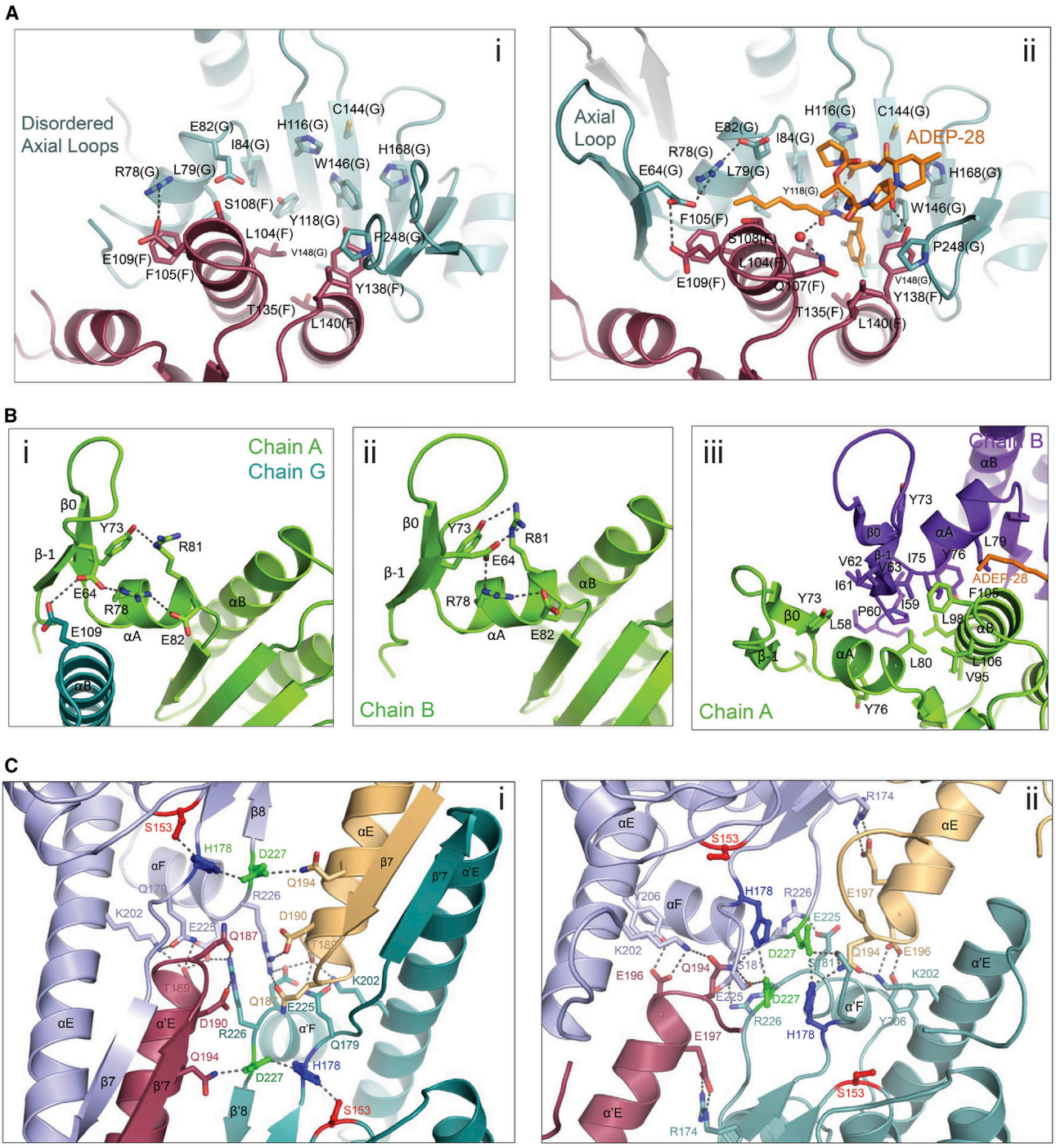

Figure 6. ADEP Binding Causes Structural Rearrangements within the HsClpP Cylinder

(A) Local molecular interactions at the binding pocket between adjacent HsClpP subunits F and G in the absence of ADEP are shown in (i). Local molecular interactions between ADEP-28 and residues in the binding pocket between two adjacent HsClpP subunits F and G are shown in (ii). ADEP-28 and the amino acid residues of interest are shown as sticks. Non-covalent bonds are indicated by dotted lines. The axial loop is indicated.

(B) ADEP-28 binding induces the ordering of N-terminal axial pore loops into β hairpins due to interactions shown in panels i, ii, and iii and discussed in the text.

(C) Molecular interactions at the equatorial plane of apo and ADEP-28-bound HsClpP. The different HsClpP subunits are distinguished by color. All the relevant amino acid residues are shown as sticks, with the catalytic triad residues S153, H178, and D227 colored in red, blue, and green, respectively. Secondary structures of each HsClpP subunit are labeled as shown, with subunits from the opposite ring denoted with the prime mark (′). Non-covalent bonds between residues are indicated by dotted lines.

β0 strands are highly structured in all subunits, segments of the β-hairpin loops formed by residues 65–69 in subunits C to G have ambiguous electron density insufficient to confidently assign side-chain positions. These residues have significantly higher *B* factors than those of the rest of the HsClpP molecule (Figure 5E), suggesting greater flexibility. Each axial β hairpin is anchored to the head domain of the same subunit through the interactions of E64 on β-1 strand and Y73 on β0 strand with R78 and R81 on αA helix, respectively (Figure 6Bi, ii). The continuous stretch of seven hydrophobic residues (L58 to V63) comprising the short N-terminal loop and the β1 strand form hydrophobic interactions with an extensive surface formed by Y73 (β0), Y76 (αA), L80 (αA), V95 (αB), L98 (αB), F105 (αB), and L106 (αB) of a neighboring subunit, and I75 (αA) and Y76 (αA) of the same subunit (Figure 6Biii). These interactions result in the retraction of the N terminus away from the 7-fold axis, leading to HsClpP's axial pore widening. This has also been observed to occur in ADEP-bound EcClpP (Li et al., 2010).

The compaction of the ADEP-28-HsClpP complex was unexpected and is a direct consequence of molecular rearrangements at and around the handle region composed mainly of β7 and αE, resulting in significant reshuffling of the residues at the interface of the two apposing HsClpP rings (Figure 6Ci, ii). At the subunit level, residues 182–187 (182–191 in chain B) that are part of β7 strand of the handle region in apo HsClpP show no clear electron density upon ADEP-28 binding, suggesting local structural disorder of the handle region (Figure 6Cii). Furthermore, the ensuing αE helix is shortened by the unwinding of two helical turns to an ordered loop that extends into HsClpP's lumen due to a kink that starts at residue Q194 (Figure 6Cii).

In apo HsClpP, the interface of two heptameric rings consists of an intricate network of H bonding and ionic interactions. The highly conserved oligomerization sensor R226 (αF-β8 loop) participates in intra-ring interactions with Q187 (β7-αE loop) and D190 (αE) of a neighboring subunit and in inter-ring interactions with E225 (α′F) of the apposing subunit (Figure 6Ci). Residues Q179 (β6-β7 loop) and K202 (αE) also form H bonds with T189 (α′E) of the apposing subunit. Residue Q194 (αE) forms an H bond with the catalytic D227 residue (in green) of a neighboring subunit to further cement intra-ring subunit contacts (Figure 6Ci). These interactions are conserved and highly symmetrical across the equatorial region of the HsClpP tetradecamer and are likely essential for a properly aligned catalytic triad (S153, H178, D227).

In ADEP-28-bound HsClpP, significant rearrangements of the intra- and inter-ring contacts occur as the long αF-β8 loops of apposing subunits come closer together to form part of the new interface. Remarkably, the catalytic triads become distorted as a result, such that H178 of one subunit now interacts with D227 of the apposing subunit and vice versa, while the original intra-subunit interaction between H178 and S153 and the inter-subunit interaction between D227 of one subunit with Q194 of the adjacent subunit are both lost (Figure 6Cii). His178 forms a bond with Q194 of an apposing subunit while D227 forms a bond with S181 of another apposing subunit. Furthermore, new intra-ring and inter-ring contacts are borne out of this structural rearrangement. These include the R174 (β6)-E197 (α′E) ionic interaction, the interactions of residues K202 and Y206 in α′E with Q194 and E196 of the apposing subunit, and the bond between S181 (β6-β7 loop) and the catalytic D227 of the apposing ring. Interestingly, despite these major changes at the interface, the inter-ring interaction of R226 in one subunit with E225 of the apposing subunit is preserved, albeit with a shift in the relative positions of the residues (Figure 6Cii). The overall result of these molecular rearrangements is the compaction of the HsClpP tetradecamer.

Compaction of HsClpP Results in the Formation of Equatorial Side Pores

This structure of ADEP-bound HsClpP highlights an unexpected role of the catalytic triad residues in stabilizing the compact conformation. Several distinct, compact conformations have been observed in the crystal structures of ClpP from *E. coli* (Kimber et al., 2010), *Listeria monocytogenes* (Zeiler et al., 2013), *M. tuberculosis* (Ingvarsson et al., 2007), *Plasmodium falciparum* (El Bakkouri et al., 2010), *Staphylococcus aureus* (Ye et al., 2013), and *Streptococcus pneumoniae* (Gribun et al., 2005) (Figure S5). In addition, SaClpP was also crystallized in a compressed conformation (Zhang et al., 2011). We define the compact conformation as a shortened ClpP cylinder losing one or more turns at the N terminus of the αE helix and in many cases concomitant with the loss of density for the β7 strand. The compressed conformation refers to an even shorter ClpP cylinder caused by a kink in the αE helix, resulting in the formation of two smaller helices.

These ClpP structures (Figure S5) have varying degrees of compaction with the distorted catalytic triads engaging in distinct interactions with nearby residues. Among these, the LmClpP1 and SaClpP compact structures show engagement of one or more of the catalytic triad residues in inter-ring interactions (Figure S5) as does the compact ADEP-28-HsClpP structure (Figure 6ii), albeit having different interacting residues. The compressed SaClpP shows inter-ring interactions of the catalytic triad but are mediated by a sulfate group (Figure S5).

The compact structure of ADEP-28-HsClpP exhibits small, equatorial side pores that presumably enlarge to facilitate the egress of cleaved peptides from the ClpP barrel (Figure S6A). These are in close proximity to the peptide substrate binding site and are formed by residues in the vicinity of the hinge region. Other compact ClpP structures exhibit equatorial side pores of varying sizes and shapes depending on the degree of compaction (Figure S6B). Interestingly, in the compact ADEP-28-HsClpP, the unraveling of two N-terminal helical turns of the αE helix results in a structured loop (spanning residues 188–194), a segment of which occupies the location of the bound peptide substrate near the catalytic site and the side pore (Figure S6A). A similar phenomenon is observed in the compact structure of PfClpP as well as in the compressed structure of SaClpP, where the αE helix is kinked in such a way that the ensuing residues of a short loop occupy the peptide-binding site. Therefore, the compact and compressed structures of ClpP are likely intermediates that are populated during ClpP's functional cycle during which a cleaved peptide is poised for release from the ClpP lumen through the equatorial side pores.

Analysis of the available ClpP structures from different species where both extended and compact conformations have been solved shows that the seven catalytic Ser residues of a ClpP heptameric ring form a plane that is parallel to that formed by

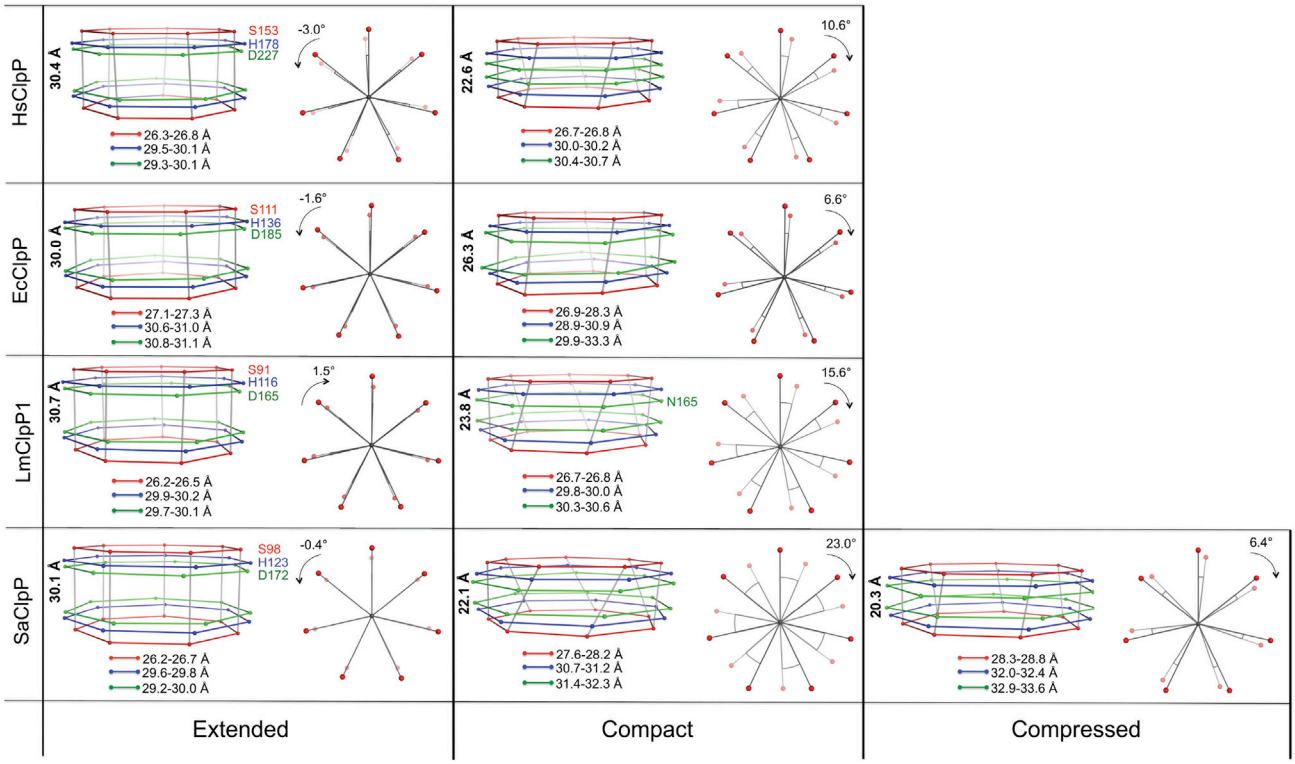

Figure 7. Putative Intermediates in the ClpP Functional Cycle Represented by Various ClpP Structures from Different Species

Shown are the relative positions of the Ser-His-Asp catalytic triads in the extended and compact structures of ClpP from different species. The PDB IDs for the extended HsClpP, EcClpP, LmClpP1, and SaClpP are PDB: 1TG6, 1YG6, 4JCR, and 3STA, respectively, while those for the compact are: this study, PDB: 3HLN, 4JCQ, and 4EMM, respectively. Also, there is a compressed structure of SaClpP with PDB: 3ST9. Note that the compact state of EcClpP was the result of the introduction of disulfide bond between two αE helices of apposing rings due to the mutation of A153 to Cys. For LmClpP1, the WT protein has Asn instead of Asp in the catalytic triad (residue 165) and is in the compact state. The N165D mutant adopts the extended state. The Cα atoms of the catalytic Ser, His, and Asp are shown as red, blue, and green spheres. The distances between the different Cα atoms are shown as lines in the respective colors. The numbers on the left refer to the distance between the plane formed by the Ser Cα atoms of one heptamer relative to the plane formed by the Ser Cα atoms in the apposing heptamer.

the other seven catalytic Ser residues in the apposing heptamer (rotation angle, $\theta = -3^\circ$ to $+1.5^\circ$) (Figure 7). The distance between each plane's center of mass (with each plane defined by the coordinates of the Ser Cα atoms) is ~30 Å, and this "height" decreases by as much as 8 Å upon compaction. Compaction is accompanied by rotation of the catalytic Ser planes relative to each other by as much as 23° and a concomitant, general increase in the distances between the seven coplanar Ser residues of a ring (Figure 7). The same is true for the other catalytic residues. For SaClpP where a third, compressed structure is available, the "height" is further reduced to ~20 Å, while the rotation angle between catalytic Ser planes is reduced to just 6.4°, presumably to relieve the strain caused by compression (Figure 7). Thus, collectively, these ClpP structures may constitute distinct structural intermediates in the conformational landscape of ClpP, whether as a result of activation by ADEP or ClpX or by natural breathing motions.

Solution Structure of ADEP-Bound HsClpP Characterized by Small-Angle X-Ray Scattering

The global conformational change in the HsClpP structure upon ADEP binding was further examined in solution using small-angle X-ray scattering (SAXS) (Figure S7A). HsClpP, HsClpP + DMSO (control for DMSO's effect), and HsClpP + ADEP-28 showed molecular mass (MM) values that correspond to tetradecamers (Table S4). The small increase in MM for HsClpP + ADEP-28 suggested that ADEP-28 molecules were bound to HsClpP. Pair distance distribution functions, p(r), were then generated (Figure S7B) and the values for the radius of gyration (R_g) and maximum dimension (D_{max}) were determined. HsClpP and HsClpP + DMSO showed similar p(r) profiles (Figure S7B), and also similar R_g and D_{max} values (Table S4). All values were in agreement with the calculated size and dimensions of HsClpP's crystallographic structure. Importantly, the addition of ADEP-28 changed HsClpP's p(r) profile, shifting the maximum p(r) and D_{max} toward higher values (Figure S7B).

Using SAXS data, we generated low-resolution dummy atoms models (DAMs) for HsClpP + DMSO and HsClpP + ADEP-28 (Figure S7C). Notably, in the presence of DMSO, HsClpP adopts a cylindrical shape in solution that is compatible with the published structure of apo HsClpP (Kang et al., 2004). The ADEP-bound HsClpP DAM showed an increased radial and axial occupancy with DAMs, adopting an ellipsoidal shape. The superposition of our ADEP-bound HsClpP crystallographic structure on this DAM (Figure S7C) showed a good fit at radial positions, supporting the existence of this compact

conformation. Nevertheless, the empty spaces observed at the top and bottom regions of the ADEP-bound HsClpP DAM, and the differences between properties calculated from the crystal structure and determined from the SAXS data (Table S4), indicate the likely presence of other HsClpP conformers in solution.

DISCUSSION

We have presented the first detailed biochemical and biophysical characterization of the molecular interactions between ADEP and mitochondrial HsClpP, as well as the first report on the physiological impact of these interactions on human cells. Indeed, Lowth et al. (2012) had reported earlier that some ADEP analogs that they tested also affected HsClpP, although they did not characterize those interactions further. Our identification of ADEPs that activate HsClpP was a fortuitous finding stemming from our work on developing antibiotics targeting the bacterial ClpP.

The co-crystal structure of the ADEP-28 and HsClpP recapitulates previous findings in ADEP-bound bacterial ClpPs, while providing further insights into the protease's functional cycle. Notably, the compact conformation of the ADEP-28-HsClpP complex may constitute a putative intermediate state. Theoretical, biochemical, and biophysical experiments have pointed toward a dynamic ClpP tetradecamer that can extend, compact, and compress (Kimber et al., 2010; Liu et al., 2014). The structure of ADEP-28-HsClpP highlights the essential role of the handle region to achieve a compact conformation while bound by ADEP-28 at the activator site, providing the first structural evidence that an ADEP-activated ClpP is not locked in the extended conformation, contrary to the proposal by Gersch et al. (2015). Remarkably, the X-ray structure also unveils a previously unknown structural role for the catalytic triad outside of proteolysis that appears essential for stabilizing the compact conformation.

Importantly, the interaction of ADEP with HsClpP produces a cytotoxic effect on cells that manifests via the intrinsic, caspase-dependent apoptosis. An important practical implication of this finding is the potential use of ADEPs as therapeutic compounds for cancer treatment. Modulation of the cell's sensitivity to ADEPs by intracellular HsClpP expression enables the fine-tuning of the ADEP chemical structure, such that new analogs can be developed with better abilities to distinguish and target cancer cells that express high levels of HsClpP without affecting normal, healthy cells. To this end, our biophysical and structural data on the interaction between ADEP and HsClpP should prove valuable in identifying key chemical features in the ADEP structure that define its potency, and should facilitate the design of better analogs.

SIGNIFICANCE

The mitochondrion is a vital organelle in the human cell that has many essential biological functions. These include energy metabolism, signaling, and apoptosis. Consequently, a dysfunctional mitochondrion may give rise to a wide range of diseases including cancer. In this work, we describe the identification of compounds that dysregulate the activity of a critical protease present in the mitochondrial matrix termed ClpP. These compounds dysregulate the protease activity of ClpP and cause it to unspecifically degrade proteins in the mitochondrion, leading to apoptotic cell death. We also obtained the co-crystal structure of ClpP with one of these compounds, revealing a different conformation for the protease. We propose that such compounds can be further developed to target cancer cells.

STAR★METHODS

Detailed methods are provided in the online version of this paper and include the following:

- KEY RESOURCES TABLE
- CONTACT FOR REAGENT AND RESOURCE SHARING
- EXPERIMENTAL MODEL AND SUBJECT DETAILS
  - Bacterial Cell Cultures
  - Mammalian Cell Cultures
- METHOD DETAILS
  - Molecular Cloning and Protein Purification
  - Screen of ADEP Analogs Against HsClpP
  - Peptidase Activity Assays
  - Protease Activity Assays
  - X-Ray Structure Determination of ADEP-28-HsClpP
  - Small Angle X-Ray Scattering (SAXS) Experiments
  - Testing the Effect of Adeps on Different Cell Lines
  - Mitochondrial Proteome Profiling for WT and *CLPP*$^{-/-}$
  - Light and Fluorescence Microscopy
  - 3D Structured Illumination Microscopy (3DSIM)
  - Western Blots
  - Cellular Respiration Analysis
- QUANTIFICATION AND STATISTICAL ANALYSIS
- DATA AND SOFTWARE AVAILABILITY

SUPPLEMENTAL INFORMATION

Supplemental Information includes seven figures and four tables and can be found with this article online at https://doi.org/10.1016/j.chembiol.2018.05.014.

ACKNOWLEDGMENTS

We thank Sheena Garcia (University of Toronto) for help with the purification of HsClpP and Dr. Christopher Tsu (Millennium Pharmaceuticals, USA) for advice on the peptidase assays. We also thank Drs. Aiping Dong and Wolfram Tempel of the Structural Genomics Consortium (SGC), University of Toronto for their help with the collection of the diffraction data. T.V.S. was supported by CNPq-Brazil fellowship (202192/2015-6) and a Saskatchewan Health Research Foundation postdoctoral fellowship. Y.-Q.M. was supported by a fellowship from the Center for Pharmaceutical Oncology (University of Toronto). K.R. was supported by a Canadian Institutes of Health Research (CIHR) Training Program in Protein Folding and Interaction Dynamics: Principles and Diseases fellowship (TGF-53910) and by a University of Toronto Fellowship from the Department of Biochemistry. A.M. is a recipient of an Ontario Trillium Scholarship. This work was funded by Natural Sciences and Engineering Research Council of Canada (NSERC) grant (RGPIN 2014-05393) to W.A.H., Global Affairs Canada (Canada) and CAPES (Brazil) to W.A.H. and C.H.I.R., CIHR (RSN-124512, MOP-125952, RSN-132191, and FDN-154318) to M.B. who also holds a CIHR New Investigator award, and NSERC (RGPIN 2015–04795) to V.M. Funding was also received from CIHR Emerging Team Grants from the Institute of Infection and Immunity (XNE-86945) to R.A.B. and W.A.H. This work was partially supported by FAPESP (2015/15822-1, 2012/01953-9, 2016/05019-0) and CNPq to L.R.S.B., who also holds a research fellowship from CNPq (306943/2015-8, 420567/2016-0). C.H.I.R.

has a research fellowship from CNPq and FAPESP (2012/50161-8, 2015/15822-1). SGC is a registered charity (no. 1097737) funded by AbbVie, Bayer Pharma, Boehringer Ingelheim, Canada Foundation for Innovation, Eshelman Institute for Innovation, and Genome Canada through Ontario Genomics Institute, Innovative Medicines Initiative (EU/EFPIA; ULTRA-DD grant no. 115766), Janssen, Merck & Co., Novartis Pharma, Ontario Ministry of Economic Development and Innovation, Pfizer, São Paulo Research Foundation - FAPESP, Takeda, and the Wellcome Trust.

AUTHOR CONTRIBUTIONS

The majority of the biochemical and cell biological experiments were performed by K.S.W. under the supervision of W.A.H. The ADEP analogs were synthesized by J.G. under the supervision of R.A.B. Initial screens for ADEP analogs were performed by E.L. X-ray crystallography and analysis of the structure of the ADEP-bound HsClpP were performed by M.F.M. SAXS experiments and data analyses were performed by T.V.S. with help from K.R., L.R.S.B., and C.H.I.R. M.T.M., L.H., and S.P. performed mitochondrial isolation, whole proteome profiling, and mass spectrometry data analyses under the supervision of M.B. 3DSIM imaging was performed by A.M. under the supervision of V.M. Cell lines that overexpress HsClpP were constructed by Y.-Q.M. A.D.S. advised on the cell-based assays. W.A.H., K.S.W., and M.F.M. wrote the manuscript with the help of the other authors.

DECLARATION OF INTERESTS

The authors declare no competing interests.

Received: December 8, 2017
Revised: April 14, 2018
Accepted: May 18, 2018
Published: June 28, 2018

REFERENCES

Adams, P.D., Afonine, P.V., Bunkoczi, G., Chen, V.B., Davis, I.W., Echols, N., Headd, J.J., Hung, L.W., Kapral, G.J., Grosse-Kunstleve, R.W., et al. (2010). PHENIX: a comprehensive Python-based system for macromolecular structure solution. Acta Crystallogr. D Biol. Crystallogr. *66*, 213–221.

Alexopoulos, J.A., Guarne, A., and Ortega, J. (2012). ClpP: a structurally dynamic protease regulated by AAA+ proteins. J. Struct. Biol. *179*, 202–210.

Amor, A.J., Schmitz, K.R., Sello, J.K., Baker, T.A., and Sauer, R.T. (2016). Highly dynamic interactions maintain kinetic stability of the ClpXP protease during the ATP-fueled mechanical cycle. ACS Chem. Biol. *11*, 1552–1560.

Barbosa, L.R.S., Spinozzi, F., Mariani, P., and Itri, R. (2013). Small-angle x-ray scattering applied to proteins in solution. In Proteins in Solution and at Interfaces: Methods and Applications in Biotechnology and Materials Science, J.M. Ruso and Á. Piñeiro, eds. (Wiley), pp. 49–72.

Bewley, M.C., Graziano, V., Griffin, K., and Flanagan, J.M. (2006). The asymmetry in the mature amino-terminus of ClpP facilitates a local symmetry match in ClpAP and ClpXP complexes. J. Struct. Biol. *153*, 113–128.

Bram, E., Ifergan, I., Shafran, A., Berman, B., Jansen, G., and Assaraf, Y.G. (2006). Mutant Gly482 and Thr482 ABCG2 mediate high-level resistance to lipophilic antifolates. Cancer Chemother. Pharmacol. *58*, 826–834.

Brötz-Oesterhelt, H., Beyer, D., Kroll, H.P., Endermann, R., Ladel, C., Schroeder, W., Hinzen, B., Raddatz, S., Paulsen, H., Henninger, K., et al. (2005). Dysregulation of bacterial proteolytic machinery by a new class of antibiotics. Nat. Med. *11*, 1082–1087.

Calvo, S.E., Clauser, K.R., and Mootha, V.K. (2016). MitoCarta2.0: an updated inventory of mammalian mitochondrial proteins. Nucleic Acids Res. *44*, D1251–D1257.

Carney, D.W., Schmitz, K.R., Truong, J.V., Sauer, R.T., and Sello, J.K. (2014). Restriction of the conformational dynamics of the cyclic acyldepsipeptide antibiotics improves their antibacterial activity. J. Am. Chem. Soc. *136*, 1922–1929.

Cole, A., Wang, Z., Coyaud, E., Voisin, V., Gronda, M., Jitkova, Y., Mattson, R., Hurren, R., Babovic, S., Maclean, N., et al. (2015). Inhibition of the mitochondrial protease ClpP as a therapeutic strategy for human acute myeloid leukemia. Cancer Cell *27*, 864–876.

Cong, L., Ran, F.A., Cox, D., Lin, S., Barretto, R., Habib, N., Hsu, P.D., Wu, X., Jiang, W., Marraffini, L.A., et al. (2013). Multiplex genome engineering using CRISPR/Cas systems. Science *339*, 819–823.

Csizmadia, V., Hales, P., Tsu, C., Ma, J., Chen, J., Shah, P., Fleming, P., Senn, J.J., Kadambi, V.J., Dick, L., et al. (2016). Proteasome inhibitors bortezomib and carfilzomib used for the treatment of multiple myeloma do not inhibit the serine protease HtrA2/Omi. Toxicol. Res. *5*, 1619–1628.

El Bakkouri, M., Pow, A., Mulichak, A., Cheung, K.L., Artz, J.D., Amani, M., Fell, S., de Koning-Ward, T.F., Goodman, C.D., McFadden, G.I., et al. (2010). The Clp chaperones and proteases of the human malaria parasite Plasmodium falciparum. J. Mol. Biol. *404*, 456–477.

Elmore, S. (2007). Apoptosis: a review of programmed cell death. Toxicol. Pathol. *35*, 495–516.

Emsley, P., and Cowtan, K. (2004). Coot: model-building tools for molecular graphics. Acta Crystallogr. D Biol. Crystallogr. *60*, 2126–2132.

Fischer, F., Hamann, A., and Osiewacz, H.D. (2012). Mitochondrial quality control: an integrated network of pathways. Trends Biochem. Sci. *37*, 284–292.

Gersch, M., Famulla, K., Dahmen, M., Gobl, C., Malik, I., Richter, K., Korotkov, V.S., Sass, P., Rubsamen-Schaeff, H., Madl, T., et al. (2015). AAA+ chaperones and acyldepsipeptides activate the ClpP protease via conformational control. Nat. Commun. *6*, 6320.

Goodreid, J.D., Janetzko, J., Santa Maria, J.P., Jr., Wong, K.S., Leung, E., Eger, B.T., Bryson, S., Pai, E.F., Gray-Owen, S.D., Walker, S., et al. (2016). Development and characterization of potent cyclic acyldepsipeptide analogues with increased antimicrobial activity. J. Med. Chem. *59*, 624–646.

Gribun, A., Kimber, M.S., Ching, R., Sprangers, R., Fiebig, K.M., and Houry, W.A. (2005). The ClpP double ring tetradecameric protease exhibits plastic ring-ring interactions, and the N termini of its subunits form flexible loops that are essential for ClpXP and ClpAP complex formation. J. Biol. Chem. *280*, 16185–16196.

Ingvarsson, H., Mate, M.J., Hogbom, M., Portnoi, D., Benaroudj, N., Alzari, P.M., Ortiz-Lombardia, M., and Unge, T. (2007). Insights into the inter-ring plasticity of caseinolytic proteases from the X-ray structure of mycobacterium tuberculosis ClpP1. Acta Crystallogr. D Biol. Crystallogr. *63*, 249–259.

Kang, S.G., Maurizi, M.R., Thompson, M., Mueser, T., and Ahvazi, B. (2004). Crystallography and mutagenesis point to an essential role for the N-terminus of human mitochondrial ClpP. J. Struct. Biol. *148*, 338–352.

Kang, S.G., Ortega, J., Singh, S.K., Wang, N., Huang, N.N., Steven, A.C., and Maurizi, M.R. (2002). Functional proteolytic complexes of the human mitochondrial ATP-dependent protease, hClpXP. J. Biol. Chem. *277*, 21095–21102.

Kim, D.Y., and Kim, K.K. (2008). The structural basis for the activation and peptide recognition of bacterial ClpP. J. Mol. Biol. *379*, 760–771.

Kimber, M.S., Yu, A.Y., Borg, M., Leung, E., Chan, H.S., and Houry, W.A. (2010). Structural and theoretical studies indicate that the cylindrical protease ClpP samples extended and compact conformations. Structure *18*, 798–808.

Kroemer, G., and Reed, J.C. (2000). Mitochondrial control of cell death. Nat. Med. *6*, 513–519.

Landes, T., and Martinou, J.C. (2011). Mitochondrial outer membrane permeabilization during apoptosis: the role of mitochondrial fission. Biochim. Biophys. Acta *1813*, 540–545.

Lee, B.G., Park, E.Y., Lee, K.E., Jeon, H., Sung, K.H., Paulsen, H., Rubsamen-Schaeff, H., Brötz-Oesterhelt, H., and Song, H.K. (2010). Structures of ClpP in complex with acyldepsipeptide antibiotics reveal its activation mechanism. Nat. Struct. Mol. Biol. *17*, 471–478.

Lee, C.D., Sun, H.C., Hu, S.M., Chiu, C.F., Homhuan, A., Liang, S.M., Leng, C.H., and Wang, T.F. (2008). An improved SUMO fusion protein system for effective production of native proteins. Protein Sci. *17*, 1241–1248.

Leung, E., Datti, A., Cossette, M., Goodreid, J., McCaw, S.E., Mah, M., Nakhamchik, A., Ogata, K., El Bakkouri, M., Cheng, Y.Q., et al. (2011). Activators of cylindrical proteases as antimicrobials: identification and

development of small molecule activators of ClpP protease. Chem. Biol. *18*, 1167–1178.

Li, D.H., Chung, Y.S., Gloyd, M., Joseph, E., Ghirlando, R., Wright, G.D., Cheng, Y.Q., Maurizi, M.R., Guarne, A., and Ortega, J. (2010). Acyldepsipeptide antibiotics induce the formation of a structured axial channel in ClpP: a model for the ClpX/ClpA-bound state of ClpP. Chem. Biol. *17*, 959–969.

Liu, K., Ologbenla, A., and Houry, W.A. (2014). Dynamics of the ClpP serine protease: a model for self-compartmentalized proteases. Crit. Rev. Biochem. Mol. Biol. *49*, 400–412.

Lo, J.H., Baker, T.A., and Sauer, R.T. (2001). Characterization of the N-terminal repeat domain of Escherichia coli ClpA—a class I Clp/HSP100 ATPase. Protein Sci. *10*, 551–559.

Lowth, B.R., Kirstein-Miles, J., Saiyed, T., Brötz-Oesterhelt, H., Morimoto, R.I., Truscott, K.N., and Dougan, D.A. (2012). Substrate recognition and processing by a Walker B mutant of the human mitochondrial AAA+ protein CLPX. J. Struct. Biol. *179*, 193–201.

McIlwain, D.R., Berger, T., and Mak, T.W. (2013). Caspase functions in cell death and disease. Cold Spring Harb. Perspect. Biol. *5*, a008656.

Mylonas, E., and Svergun, D.I. (2007). Accuracy of molecular mass determination of proteins in solution by small-angle X-ray scattering. J. Appl. Crystallogr. *40*, s245–s249.

Nunnari, J., and Suomalainen, A. (2012). Mitochondria: in sickness and in health. Cell *148*, 1145–1159.

Olivares, A.O., Baker, T.A., and Sauer, R.T. (2016). Mechanistic insights into bacterial AAA+ proteases and protein-remodelling machines. Nat. Rev. Microbiol. *14*, 33–44.

Otwinowski, Z., and Minor, W. (1997). Processing of x-ray diffraction data collected in oscillation mode. In Macromolecular Crystallography, Part A, C.W. Carter, Jr. and R.M. Sweet, eds. (Academic Press), pp. 307–326.

Petoukhov, M.V., Franke, D., Shkumatov, A.V., Tria, G., Kikhney, A.G., Gajda, M., Gorba, C., Mertens, H.D., Konarev, P.V., and Svergun, D.I. (2012). New developments in the ATSAS program package for small-angle scattering data analysis. J. Appl. Crystallogr. *45*, 342–350.

Pettersen, E.F., Goddard, T.D., Huang, C.C., Couch, G.S., Greenblatt, D.M., Meng, E.C., and Ferrin, T.E. (2004). UCSF Chimera—a visualization system for exploratory research and analysis. J. Comput. Chem. *25*, 1605–1612.

Schmitz, K.R., Carney, D.W., Sello, J.K., and Sauer, R.T. (2014). Crystal structure of Mycobacterium tuberculosis ClpP1P2 suggests a model for peptidase activation by AAA+ partner binding and substrate delivery. Proc. Natl. Acad. Sci. USA *111*, E4587–E4595.

Seiferling, D., Szczepanowska, K., Becker, C., Senft, K., Hermans, S., Maiti, P., Konig, T., Kukat, A., and Trifunovic, A. (2016). Loss of CLPP alleviates mitochondrial cardiomyopathy without affecting the mammalian UPRmt. EMBO Rep. *17*, 953–964.

Selleck, W., and Tan, S. (2008). Recombinant protein complex expression in *E. coli*. Curr. Protoc. Protein Sci. *Chapter 5*. Unit 5.21.

Seo, J.H., Rivadeneira, D.B., Caino, M.C., Chae, Y.C., Speicher, D.W., Tang, H.Y., Vaira, V., Bosari, S., Palleschi, A., Rampini, P., et al. (2016). The mitochondrial unfoldase-peptidase complex ClpXP controls bioenergetics stress and metastasis. PLoS Biol. *14*, e1002507.

Szczepanowska, K., Maiti, P., Kukat, A., Hofsetz, E., Nolte, H., Senft, K., Becker, C., Ruzzenente, B., Hornig-Do, H.T., Wibom, R., et al. (2016). CLPP coordinates mitoribosomal assembly through the regulation of ERAL1 levels. EMBO J. *35*, 2566–2583.

Wojtyra, U.A., Thibault, G., Tuite, A., and Houry, W.A. (2003). The N-terminal zinc binding domain of ClpX is a dimerization domain that modulates the chaperone function. J. Biol. Chem. *278*, 48981–48990.

Ye, F., Zhang, J., Liu, H., Hilgenfeld, R., Zhang, R., Kong, X., Li, L., Lu, J., Zhang, X., Li, D., et al. (2013). Helix unfolding/refolding characterizes the functional dynamics of *Staphylococcus aureus* Clp protease. J. Biol. Chem. *288*, 17643–17653.

Zeiler, E., List, A., Alte, F., Gersch, M., Wachtel, R., Poreba, M., Drag, M., Groll, M., and Sieber, S.A. (2013). Structural and functional insights into caseinolytic proteases reveal an unprecedented regulation principle of their catalytic triad. Proc. Natl. Acad. Sci. USA *110*, 11302–11307.

Zhang, J., Ye, F., Lan, L., Jiang, H., Luo, C., and Yang, C.G. (2011). Structural switching of Staphylococcus aureus Clp protease: a key to understanding protease dynamics. J. Biol. Chem. *2a86*, 37590–37601.

STAR★METHODS

KEY RESOURCES TABLE

REAGENT or RESOURCE	SOURCE	IDENTIFIER
Antibodies		
Mouse monoclonal anti-HsClpP	Abcam	RRID: AB_941071
Rabbit polyclonal anti-HsClpX	Abcam	RRID: AB_11000791
Mouse monoclonal anti-GAPDH	Abcam	RRID: AB_2107448
Rabbit polyclonal anti-Caspase-8	Cell Signaling Technology	RRID: AB_10545768
Rabbit polyclonal anti-Caspase-9	Cell Signaling Technology	RRID: AB_2068621
Rabbit monoclonal anti-PUMA	Cell Signaling Technology	RRID: AB_2064551
Goat polyclonal anti-Caspase-3	R&D Biosystems	RRID: AB_354518
Mouse monoclonal anti-Mcl-1	EMD Millipore	RRID: AB_10806351
Mouse monoclonal anti-Bcl2	EMD Millipore	RRID: AB_11210561
Mouse monoclonal anti-FLAG-tag	Sigma-Aldrich	RRID: AB_262044
HRP-conjugated goat anti-rabbit IgG	BioRad	RRID: AB_11125142
HRP-conjugated goat anti-mouse IgG	BioRad	RRID: AB_11125547
HRP-conjugated rabbit anti-goat IgG	Sigma-Aldrich	RRID: AB_258242
Chemicals, Peptides, and Recombinant Proteins		
ADEP-28	(Goodreid et al., 2016)	N/A
ADEP-41	(Goodreid et al., 2016)	N/A
ADEP-06	(Goodreid et al., 2016)	N/A
ADEP-02	(Goodreid et al., 2016)	N/A
ADEP-04	(Goodreid et al., 2016)	N/A
Other ADEP analogs, see Table S1	(Goodreid et al., 2016)	N/A
N-acetyl-Trp-Leu-Ala-7-amido-4-methylcoumarin	R&D Biosystems	Cat#S-330-02M
Benzyloxycarbonyl-Arg-Arg-7-amido-4-methylcoumarin	Sigma-Aldrich	Cat#C5429
N-acetyl-Leu-Glu-His-Asp-7-amido-4-methylcoumarin	Sigma-Aldrich	Cat#SCP0104
N-acetyl-Val-Glu-Thr-Asp-7-amido-4-methylcoumarin	Sigma-Aldrich	Cat#SCP0139
Benzyloxycarbonyl-Leu-Leu-Leu-7-amido-4-methylcoumarin	Sigma-Aldrich	Cat#C0608
N-succinyl-Leu-Tyr-7-amido-4-methylcoumarin	MP Biochemicals	Cat#03AMC117
C-terminal His6-tagged Human mitochondrial ClpP (HsClpP-His_6)	(Kimber et al., 2010)	N/A
Untagged human mitochondrial ClpP (HsClpP)	This paper	N/A
Untagged human mitochondrial ClpX (HsClpX)	This paper	N/A
Escherichia coli ClpA (EcClpA)	(Lo et al., 2001)	N/A
Escherichia coli ClpP (EcClpP)	(Wojtyra et al., 2003)	N/A
Yeast SUMO protease	(Lee et al., 2008)	N/A
Casein fluorescein isothiocyanate from bovine milk (Casein-FITC)	Sigma-Aldrich	Cat#C3777-25MG
Bovine milk α-casein	Sigma-Aldrich	Cat#C6780-1G
Creatine phosphate	Sigma-Aldrich	Cat#27920
Creatine phosphokinase	Sigma-Aldrich	Cat#C3755
Adenosine 5′-triphosphate disodium salt hydrate (ATP)	Sigma-Aldrich	Cat#A26209
Sulforhodamine B (SRB)	Sigma-Aldrich	Cat#230162
Critical Commercial Assays		
In Situ Cell Death Detection Kit, Fluorescein	Roche	Cat#Roche-11684795910
MitoTracker Red CMXRos	Molecular Probes	Cat# M7512

(*Continued on next page*)

Continued

REAGENT or RESOURCE	SOURCE	IDENTIFIER
Gateway LR Clonase II Enzyme Mix	Thermo-Fisher Scientific	Cat#11791020
Gateway BP Clonase II Enzyme Mix	Thermo-Fisher Scientific	Cat#11789020
Seahorse XF Cell Mitochondrial Stress Kit	Agilent	Cat#103015-100
Deposited Data		
X-ray structure: HsClpP in complex with ADEP-28	This paper	PDB: 6BBA
X-ray structure: HsClpP	(Kang et al., 2004)	PDB: 1TG6
X-ray structure: BsClpP in complex with ADEP1	(Lee et al., 2010)	PDB: 3KTI
X-ray structure: EcClpP	(Bewley et al., 2006)	PDB: 1YG6
X-ray structure: EcClpP A153C	(Kimber et al., 2010)	PDB: 3HLN
X-ray structure: EcClpP in complex with ADEP1	(Li et al., 2010)	PDB: 3MT6
X-ray structure: HpClpP in complex with peptide NVLGFTQ	(Kim and Kim, 2008)	PDB: 2ZL2
X-ray structure: LmClpP1 N65D	(Zeiler et al., 2013)	PDB: 4JCR
X-ray structure: LmClpP1	(Zeiler et al., 2013)	PDB: 4JCQ
X-ray structure: MtClpP1	(Ingvarsson et al., 2007)	PDB: 2CE3
X-ray structure: MtClpP1P2 in complex with ADEP	(Schmitz et al., 2014)	PDB: 4U0G
X-ray structure: NmClpP in complex with ADEP A54556	(Goodreid et al., 2016)	PDB: 5DKP
X-ray structure: PfClpP	(El Bakkouri et al., 2010)	PDB: 2F6I
X-ray structure: SaClpP (extended)	(Zhang et al., 2011)	PDB: 3STA
X-ray structure: SaClpP (compact)	(Ye et al., 2013)	PDB: 4EMM
X-ray structure: SaClpP (compressed)	(Zhang et al., 2011)	PDB: 3ST9
X-ray structure: SaClpP in complex with ADEP		PDB: 5VZ2
X-ray structure: SpClpP A153P	(Gribun et al., 2005)	PDB: 1Y7O
Experimental Models: Cell Lines		
HEK293 T-REx	Gift from A. Trifunovic	RRID: CVCL_U427
HEK293 T-REx *CLPP*$^{-/-}$	(Seiferling et al., 2016)	N/A
HEK293 T-REx + CLPP-FLAG	This paper	N/A
HEK293 T-REx + CLPP$_{S153A}$-FLAG	This paper	N/A
HEK293 T-REx *ΔCLPX**	This paper	N/A
HEK293 T-REx *CLPP*$^{-/-}$ *ΔCLPX**	This paper	N/A
HeLa	Gift from P. Kim	RRID: CVCL_0030
HeLa T-REx	Gift from L. Attisano	RRID: CVCL_D587
U2OS	Gift from A. Palazzo	RRID: CVCL_0042
SH-SY5Y	Gift from M. Babu	RRID: CVCL_0019
Experimental Models: Organisms/Strains		
Escherichia coli DH5α	Lab stock	NCBI: txid668369
Escherichia coli BL21(DE3) *ΔclpP*::*cat* (SG1146)	(Kimber et al., 2010)	N/A
Oligonucleotides		
CLPX Exon1 pX330 F: CACCGCGGTGCTTGTACTTGCGGCG	This paper	N/A
CLPX Exon1 pX330 R: AAACCGCCGCAAGTACAAGCACCGC	This paper	N/A
CLPX Exon1 ssODN: GGCCTCGCGGAGATGCCCAGCTGCGGTGCTT GTACTTGCGGCGCGGCGTAGGTCCGGCTCAT CACCTCCTCACTCGCCTCCGCGCAGAGA	This paper	N/A
Recombinant DNA		
pDT1668-LhclpP	(Kimber et al., 2010)	N/A
pET9a-EcClpA M168T	(Lo et al., 2001)	N/A
pET9a-EcClpP	(Wojtyra et al., 2003)	N/A

(*Continued on next page*)

Continued

REAGENT or RESOURCE	SOURCE	IDENTIFIER
pET28-Ulp1	(Lee et al., 2008)	N/A
pETSUMO	(Lee et al., 2008)	N/A
pETSUMO2-CLPP(-MTS)	This paper	N/A
pST39	(Selleck and Tan, 2008)	N/A
pST39-SUMO2-CLPX(-MTS)	This paper	N/A
pDEST-MTS-HsCLPP-3xFLAG	This paper	N/A
pDEST-MTS-HsCLPP$_{S153A}$-3xFLAG	This paper	N/A
pOG44	Thermo-Fisher Scientific	Cat#V600520
pX330	(Cong et al., 2013)	N/A
pX330-CLPX KO	This paper	N/A
Software and Algorithms		
HKL2000	(Otwinowski and Minor, 1997)	http://www.hkl-xray.com/download-instructions-hkl-2000
PHENIX	(Adams et al., 2010)	https://www.phenix-online.org/
COOT	(Emsley and Cowtan, 2004)	http://www2.mrc-lmb.cam.ac.uk/Personal/pemsley/coot/
ATSAS 2.7.2 software package	(Petoukhov et al., 2012)	https://www.embl-hamburg.de/biosaxs/manuals/atsas-2.7/install.html
UCSF Chimera software	(Pettersen et al., 2004)	https://www.cgl.ucsf.edu/chimera/
MaxQuant software 1.6.1.0	Max Planck Institute	http://www.coxdocs.org/doku.php?id=maxquant:common:download_and_installation#download_and_installation_guide
NIS-Elements Basic Research software	Nikon	https://www.nikoninstruments.com/Products/Software/NIS-Elements-Basic-Research
ZEN Black software 8.1	Carl Zeiss Microscopy	https://www.zeiss.com/microscopy/int/software-cameras.html
Wave Desktop software	Agilent	https://www.agilent.com/en/products/cell-analysis-(seahorse)/software-download-for-wave-desktop
Quantity One 1D Analysis software	BioRad	http://www.bio-rad.com/en-ca/product/quantity-one-1-d-analysis-software?ID=1de9eb3a-1eb5-4edb-82d2-68b91bf360fb
Other		
Rigaku FR-E SuperBright rotating anode generator	Structural Genomics Consortium, University of Toronto, Toronto, Canada	https://www.thesgc.org/science/crystallography
Pilatus 300K detector, SAXS1 beamline	Brazilian Synchrotron Light Laboratory, LNLS, CNPEM, Campinas, Brazil	http://www.lnls.cnpem.br/linhas-de-luz/saxs1-en/overview/
Proxeon EASY nanoLC 1000 System	Thermo-Fisher Scientific	Cat#LC120
Orbitrap Elite mass spectrometer	Thermo-Fisher Scientific	Cat#IQLAAEGAAPFADBMAZQ
Acclaim PepMap C18 column (15 cm x 50 ìm ID, 3 ìm, 100 Å)	Thermo-Fisher Scientific	https://www.thermofisher.com/order/catalog/product/160321
Eclipse 80i fluorescence microscope	Nikon	https://www.nikoninstruments.com/Products/Upright-Microscopes/Research/Eclipse-80i
X-Cite Series 120Q excitation light source	Excelitas Technologies	http://www.excelitas.com/Pages/Product/X-Cite-120Q.aspx

(*Continued on next page*)

Continued

REAGENT or RESOURCE	SOURCE	IDENTIFIER
ELYRA PS.1 superresolution microscope	Carl Zeiss Microscopy	https://www.zeiss.com/microscopy/int/products/superresolution-microscopy.html
iXon 885 EMCCD camera	Andor Technology	http://www.andor.com/cameras/ixon-emccd-camera-series
Microscope coverslips for SIM	Electron Microscopy Sciences	Cat#72230-01
Microscope glass slides for SIM	VWR	Cat#48312-401
ChemiDoc XRS+ System	BioRad	http://www.bio-rad.com/en-ca/product/chemidoc-xrs-system?ID=NINJHRKG4
Seahorse XFe96 Metabolic Flux Analyzer	Agilent	https://www.agilent.com/en/products/cell-analysis-(seahorse)/seahorse-analyzers/seahorse-xfe96-analyzer
Seahorse XFe96 Sensor Cartridge	Agilent	Cat#102416-100
Seahorse XF96 Cell Culture Microplates	Agilent	Cat#101085-004
EnSpire 2300 Multilabel Reader	Perkin-Elmer	http://www.perkinelmer.com/product/enspire-base-unit-2300-0000
96-well black flat-bottom plate	Greiner Bio-one International	Cat#655077

CONTACT FOR REAGENT AND RESOURCE SHARING

Further information and requests for resources and reagents should be directed to and will be fulfilled by the Lead Contact, Walid A. Houry (walid.houry@utoronto.ca).

EXPERIMENTAL MODEL AND SUBJECT DETAILS

Bacterial Cell Cultures

All *Escherichia coli* strains used for DNA propagation and protein expression (see Key Resources Table for details) were grown in Luria-Bertani Broth (LB; 10 g/L bio-tryptone + 5 g/L yeast extract + 10 g/L NaCl) supplemented with the appropriate antibiotics, unless stated otherwise. For DNA propagation, cells were grown at 37°C with shaking. For protein expression, cells in pre-cultures were grown 16-18 hours at 37°C with shaking. Cells in protein expression cultures were also grown at 37°C with shaking until induction of protein expression with 1 mM IPTG. The cultures were then maintained at 37°C for 3-5 hours or at 18°C for 16-18 hours.

Mammalian Cell Cultures

All mammalian cell lines used in this study are female (see Key Resources Table for details). Cell lines were maintained in Dulbecco's modified Eagle's medium (DMEM) supplemented with 10% fetal bovine serum (FBS), 2 mM L-glutamine and 100 U/mL penicillin-streptomycin, unless stated otherwise. Cells were grown and maintained in standard tissue culture plates or tissue culture flasks with ventilated caps. For DNA transfection, cells were kept in the same media but without any antibiotics at least 24 hours prior to the procedure. All cells were passaged by standard trypsinization procedures at least three times before use in any experiments.

For long-term cryogenic storage, cells were first trypsinized and re-suspended in media, followed by gradual addition of 80% FBS + 20% DMSO to a final 1:1 (v:v) ratio. The cell stocks were then transferred into cryogenic storage vials and stored in foam storage racks at -80°C for at least 24 hours before long-term storage in a liquid nitrogen storage tank. To recover cells from the frozen stocks, the frozen cells were thawed at 37°C and re-suspended in media at 9x the frozen stock's volume. The media was applied gradually to the cells to minimize osmotic shock. Cells were then collected by centrifugation and re-suspended in fresh media after which, they were transferred to tissue culture plates or ventilated tissue culture flasks for growth and maintenance as described.

METHOD DETAILS

Molecular Cloning and Protein Purification

For protein expression, *CLPP* gene was cloned without its mitochondrial targeting sequence (MTS) (residues M1-P57) into a modified *pETSUMO* vector (Lee et al., 2008) resulting in *pETSUMO2-CLPP*(*-MTS*) expressing 2x(His_6-thrombin)-SUMO-CLPP(-MTS). *CLPX* gene was also cloned without its MTS (residues M1-F64) into a modified *pST39* (Selleck and Tan, 2008) resulting in *pST39-SUMO2-CLPX*(*-MTS*) expressing 2x(His_6-thrombin)-SUMO-CLPX(-MTS). All plasmids were propagated in *E. coli* DH5α and isolated using the

PureLink Quick Plasmid Miniprep Kit (Thermo-Fisher Scientific). Linearized DNA and PCR amplification products were purified by gel extraction using the PureLink Quick Gel Extraction Kit (Thermo-Fisher Scientific).

HsClpP was expressed with a N-terminal 2x(His_6-thrombin)-SUMO tag in *E. coli* SG1146, which is BL21(DE3) *ΔclpP*::*cat* (Kimber et al., 2010). Cells transformed with *pETSUMO2-CLPP*(*-MTS*) were grown aerobically in LB + 50 μg/mL kanamycin at 37°C until OD_{600} reached ~0.6. Protein expression was then induced with 1.5 mM IPTG (Thermo-Fisher Scientific) for 3-5 hours. Cells were harvested by centrifugation, and then re-suspended in 25 mM TrisHCl, pH 7.5, 0.5 M NaCl, 10% glycerol, and 10 mM imidazole. Cells were then lysed by 2 passes on the French Press, and the cell debris was removed by centrifugation. The SUMO-tagged HsClpP was purified on Ni-NTA beads (Thermo-Fisher Scientific) using standard protocols. Subsequently, SUMO protease (Lee et al., 2008) was added to remove the N-terminal 2x(His_6-thrombin)-SUMO tag. The purified, untagged HsClpP was concentrated with an Amicon Ultra-15 centrifugal filter unit (10000 MWCO) (EMD Millipore) at 4°C, aliquoted, flash-frozen in liquid nitrogen and stored at −80°C until use. A similar protocol was used for HsClpX. All fractions collected during the purification were analyzed by SDS-PAGE. The proteins were found to be >95% pure.

For our high-throughput drug activity assays, C-terminally His_6-tagged HsClpP (HsClpP-His_6) was expressed in SG1146 transformed with pDT1668-LhclpP and purified as described in (Kimber et al., 2010). Untagged *E. coli* ClpP (EcClpP) was expressed and purified as described in (Wojtyra et al., 2003). *E. coli* ClpA (EcClpA) was expressed and purified as described in (Lo et al., 2001).

Screen of ADEP Analogs Against HsClpP

Structural analogs of acyldepsipeptide (ADEP) (Goodreid et al., 2016) that were previously developed as potential antibiotics against bacterial ClpP were screened and assessed for their ability to activate and dysregulate the protease activity of HsClpP, by measuring their relative degradation (RD) index. Note that ADEP-28 was also previously reported by Carney et al. (Carney et al., 2014). Details of the experimental protocol have been described in (Leung et al., 2011). All ADEP analogs were first screened at 25 μM, and their RD25 scores were calculated using the method described in (Leung et al., 2011) (Figure 1A). Those that achieved RD25 $\geq$ 0.87 were screened a second time at 5 μM, followed by calculation of their RD5 scores. The top analogs with RD5 $\geq$ 0.74 were screened a third time at 1 μM, followed by calculation of their RD1 scores (Figure 1B).

Peptidase Activity Assays

The peptidase activity of purified, untagged HsClpP was assessed by monitoring the degradation of peptidyl substrates labelled with a C-terminal 7-amido-4-methylcoumarin (AMC) fluorophore. As previously reported (Kang et al., 2002), HsClpP did not exhibit any observable peptidase activity towards the commonly used *N*-succinyl-Leu-Tyr-7-amido-4-methylcoumarin (Suc-LY-AMC) peptide (Figure 2A). To identify a suitable peptidyl substrate, commercially available AMC-labelled peptides were purchased and tested for degradation by HsClpP. These include *N*-acetyl-Trp-Leu-Ala-AMC (Ac-WLA-AMC) (R&D Systems) that was also previously used by Csizmadia *et al*. (Csizmadia et al., 2016), benzyloxycarbonyl-Arg-Arg-AMC (Z-RR-AMC) (Sigma-Aldrich), *N*-acetyl-Leu-Glu-His-Asp-AMC (Ac-LEHD-AMC) (Sigma-Aldrich), *N*-acetyl-Val-Glu-Thr-Asp-AMC (Ac-VETD-AMC) (Sigma-Aldrich), and benzyloxycarbonyl-Leu-Leu-Leu-AMC (Z-LLL-AMC) (Sigma-Aldrich). Suc-LY-AMC (MP Biomedicals) was also tested as a negative control. All stock solutions of the AMC-labelled peptides were prepared by dissolving the lyophilized peptides in DMSO at 90 mM or a lower concentration recommended by the manufacturer. All assays were performed in 50 mM TrisHCl, pH 8, 10 mM $MgCl_2$, 100 mM KCl, 0.02% Triton X-100 (v:v), 5% glycerol (v:v), and 1 mM DTT. HsClpP was used at 8 μM (final monomeric concentration) for the initial screening for a suitable substrate, but at 6 μM in subsequent experiments. All AMC-labelled peptides were used at the final concentration of 500 μM in the initial screen. Ac-WLA-AMC was used at the final concentration of 100 μM in all other experiments. Addition of the peptides also raised the final concentration of DMSO in the reaction mix to 3% (v:v). All reactions were carried out with 150 μL of the reaction mix per well on a 96-well black flat-bottom plate (Greiner) at 37°C. Degradation of the peptidyl substrates and subsequent release of the free AMC moiety was monitored by fluorescence with λ_{ex} = 360 nm and λ_{em} = 440 nm using the EnSpire 2300 Multilabel Reader (Perkin-Elmer) set to perform a reading every 30 s with 20 flashes. A total of 240 readings were collected for each of three independent replicates prepared for each peptidyl substrate.

Protease Activity Assays

The protease activity of purified HsClpP was assessed by monitoring the degradation of bovine milk casein labelled with fluorescein isothiocyanate (casein-FITC) (Sigma-Aldrich) in the presence of ADEP and/or purified HsClpX. All reactions were carried out in 25 mM HEPES, pH 7.5, 35 mM KCl, 25 mM $MgCl_2$, 0.03% Tween-20 (v:v), 10% glycerol (v:v), and 1 mM DTT, supplemented with 16 mM creatine phosphate and 300 μM ATP. HsClpP was used at 3 μM (final monomeric concentration) and casein-FITC was added at the final concentration of 10 μM. 13 U of creatine phosphokinase (Sigma-Aldrich) was also added for ATP regeneration. DMSO was present at 1% (v:v) final concentration in the experiments that involve the use of ADEP analogs. All reactions were carried out with 150 μL of the reaction mix per well in a 96-well black flat-bottom plate at 37°C. Degradation of casein-FITC and subsequent release of the free FITC moiety was monitored by fluorescence with λ_{ex} = 494 nm and λ_{em} = 518 nm using the EnSpire 2300 Multilabel Reader set to perform a reading every 40 s with 20 flashes. A total of 100 readings were collected in each experiment.

To investigate the casein-FITC degradation by HsClpXP, kinetic analysis was performed with HsClpP held constant at 3 μM (final monomeric concentration) and HsClpX was titrated from 0 to 18 μM (final monomeric concentration). Initial rates (v_0) were determined from data collected over three independent experiments. Non-linear regression analysis was then performed on the initial rates data using the Hill equation, as follows:

$$v_0 = \frac{V_{max}[\text{HsClpX or ADEP}]^h}{K_{0.5}^h + [\text{HsClpX or ADEP}]^h}$$

V_{max} is maximal velocity, h is the Hill coefficient, and $K_{0.5}$ is the microscopic apparent dissociation constant.

The effect of ADEP in activating HsClpP was assessed via the degradation of casein-FITC by HsClpP independent of HsClpX. All reactions were carried out with HsClpP at 3 μM (final monomeric concentration) in the same way as described above. ADEP analogs were titrated from 0-2 μM or 0-128 μM, depending on their potency. Initial rates data were collected and analyzed using the Hill equation above to determine V_{max}, h and $K_{0.5}$ for each ADEP analog. For experiments that require HsClpX in the reaction, the protein was added at 9 μM (final monomeric concentration).

For gel-based degradation assays, unlabelled bovine milk α-casein (Sigma-Aldrich; C6780-1G) was used in place of casein-FITC in the same reaction condition as before. HsClpP and HsClpX were used at 6 μM and 18 μM (both final monomeric concentrations), respectively, to ensure that sufficient amount of casein was degraded to be observable by SDS-PAGE, while maintaining the same HsClpP-to-HsClpX ratio as previously used. ATP concentration was also raised to 3 mM. As a representative analog, ADEP-28 was used at 0.1 μM and 2 μM along side a DMSO-only control. Samples were collected at designated time points and analyzed by SDS-PAGE. Casein degradation was quantified by densitometry using the Quantity One 1D Analysis Software (BioRad). Three independent experiments were performed for each concentration of ADEP-28 and the DMSO-only control.

X-Ray Structure Determination of ADEP-28-HsClpP

Purified untagged HsClpP was dialyzed against buffer containing 25 mM Bis-Tris, pH 6.5 and 3 mM dithiothreitol, concentrated to 10 mg/mL, and 750 μM of ADEP-28 was added. The solution was pre-incubated for 1 hr at 37°C. Subsequently, 0.5 μL of the protein-ADEP-28 solution was mixed with 0.5 μL of crystallization reagent (0.1 M sodium acetate trihydrate pH 4.6, 4% w/v Polyethylene glycol 4,000). The drops were equilibrated against the crystallization reagent in the reservoir at 21°C. Large crystals of HsClpP were observed within two weeks and grew to maximal dimensions within a month.

Crystals of HsClpP were cryoprotected by quick soaking in crystallization solution containing 20% glycerol and 1 mM ADEP-28, then flash-cooled in liquid nitrogen. Diffraction data were collected at the Structural Genomics Consortium-University of Toronto at 100 K and wavelength of 1.5418 Å using Rigaku FR-E SuperBright rotating anode generator. Diffraction data were indexed, integrated, and scaled in HKL2000 (Otwinowski and Minor, 1997). The structure of HsClpP complex with ADEP-28 was determined by molecular replacement using Phaser in PHENIX (Adams et al., 2010) with the published apo-HsClpP structure (PDB 1TG6) (Kang et al., 2004) as search model. The crystal asymmetric unit contained 7 subunits of HsClpP forming a single heptameric ring. The structure was refined initially in PHENIX with simulated annealing and coordinate shaking to remove model bias. Subsequent model building and refinement were performed in COOT (Emsley and Cowtan, 2004) and PHENIX (Adams et al., 2010) using translation-libration-screw (TLS) parameters with individual coordinate, occupancy and B factor optimization. The final model was refined to an R_{work}/R_{free} of 0.19/0.24 up to a resolution of 2.80 Å. The model has good geometry with >97% of amino acid residues in favored and allowed regions of the Ramachandran plot. Data collection and refinement statistics are summarized in Table S3. The PDB accession number is 6BBA.

Small Angle X-Ray Scattering (SAXS) Experiments

Data collection was performed using a Pilatus 300K detector in the SAXS1 beamline, located at the Brazilian Synchrotron Light Laboratory (LNLS, CNPEM, Campinas, Brazil). Measurements were done using a monochromatic X-ray beam (λ=1.488 Å) and sample-to-detector distance of ~1,000 mm. The scattering intensity, I(q), was detected as a function of the scattering vector (q), where $q = 4\pi \sin\theta / \lambda$ and 2θ is the scattering angle. The range for q was between 0.013 $Å^{-1}$ and 0.5 $Å^{-1}$. Samples were prepared at 0.5 mg/mL in buffer of 50 mM TrisHCl, pH 7.5, 200 mM KCl, 25 mM $MgCl_2$ and 10% glycerol. The final concentration of DMSO was kept at 2.3% (v:v) in samples containing ADEP (0.6 mM final) or DMSO only. Ten frames of 10 seconds and one frame of 300 seconds were recorded for every sample at 20°C to inspect for X-ray damage.

Data analysis was performed using software from the ATSAS 2.7.2 package (Petoukhov et al., 2012). All data curves were verified for X-ray damage and aggregation using the Guinier approximation and the PRIMUS software. Molecular weight determination was performed by comparing the forward scattering intensity I(0)-values obtained from Guinier approximation and I(0)-values determined from standard BSA samples (Barbosa et al., 2013; Mylonas and Svergun, 2007). Curves were normalized by protein concentration. The pair distance distribution functions, p(r), were generated by the GNOM software. Generation of dummy atoms models (DAMs) was performed using the SAXS curve until q = 0.2 and P72 symmetry in the simulated-annealing method implemented by the DAMMIF software. Ten DAM models were averaged using the DAMAVER package. Superimposition of crystallographic structures and DAMs was performed using the SUPCOMB program. Visualization of DAMs and generation of density maps were done using the UCSF Chimera software (Pettersen et al., 2004).

Testing the Effect of Adeps on Different Cell Lines

Different cell lines were grown and maintained in Dulbecco''s Modified Eagle Media (DMEM) (Gibco) supplemented with 10% fetal bovine serum (Gibco), 100 U/mL penicillin-streptomycin (Gibco) and 2 mM L-glutamine (Gibco) at 37°C under a moist atmosphere with 6% CO_2. All cells were passaged at least 3 times prior to use.

Cell lines used in the experiments presented here were acquired from various sources. HEK293 T-REx wild-type (WT) and HEK293 T-REx *CLPP*$^{-/-}$ cells were generous gifts from Professor Aleksandra Trifunovic (University of Cologne, Germany). HeLa (regular) cells were provided by Professor Peter Kim (Hospital for Sick Children, Canada). HeLa T-REx cells were obtained from Professor Lilianna Attisano (University of Toronto, Canada). U2OS cells were a gift from Professor Alex Palazzo (University of Toronto, Canada). Undifferentiated SH-SY5Y cells were provided by Professor Mohan Babu (University of Regina, Canada).

HEK293 T-REx + CLPP-FLAG and HEK293 T-REx + $CLPP_{S153A}$-FLAG were generated using the Flp-In System (Sigma-Aldrich). Briefly, full length *CLPP* gene that includes its native MTS was cloned as *pDEST-MTS-HsCLPP-3xFLAG* using the Gateway system (Thermo Fisher Scientific). For expressing the proteolytically inactive HsClpP, the S153A mutation was introduced into *pDEST-MTS-HsCLPP-3xFLAG* by QuikChange site-directed mutagenesis (Qiagen) to generate the *pDEST-MTS-HsCLPP*$_{S153A}$*-3xFLAG*. To generate the required cell lines expressing the FLAG-tagged HsClpP proteins, HEK293 T-REx WT cells were co-transfected with *pDEST-MTS-HsCLPP-3xFLAG* or *pDEST-MTS-HsCLPP*(*S153A*)*-3xFLAG* and *pOG44* (Thermo-Fisher Scientific), using the jetPRIME *In Vitro* DNA Transfection Reagent (Polyplus Transfection). Stable cell populations were isolated by multiple rounds of selection in media supplemented with 200 μg/mL hygromycin.

HEK293 T-REx *ΔCLPX** and HEK293 T-REx *CLPP*$^{-/-}$ *ΔCLPX** were generated by disrupting the *CLPX* gene in HEK293 T-REx WT and *CLPP*$^{-/-}$ cells, respectively, using CRISPR/Cas9 methodology as detailed in (Cong et al., 2013). Briefly, the required gRNA sequence targeting in proximity to exon 1 of *CLPX* was introduced into pX330 with the oligonucleotides CLPX Exon1 pX330 F and CLPX Exon1 pX330 R (sequence shown in Key Resources Table) via designated BbsI restriction sites. Next, the modified pX330 plasmid and the oligonucleotide CLPX Exon1 ssODN (sequence shown in Key Resources Table) were co-transfected into WT and *CLPP*$^{-/-}$ cells using Lipofectamine 2000 (Thermo-Fisher Scientific) following the manufacturer's protocol. CLPX Exon1 ssODN provides the necessary repair template after the Cas9-mediated DNA cleavage and causes omission of *CLPX*'s start codon to inhibit protein expression. The efficacy of *CLPX* disruption in suppressing HsClpX expression was assessed by Western blotting. Both WT and *CLPP*$^{-/-}$ were subjected to two additional rounds of CRISPR-Cas9 treatment in sequence to maximize the suppression of HsClpX expression.

To assess the cytotoxicity of ADEP analogs, cells were seeded at 1 x 10^3 or 2 x 10^3 cells in 50 μL per well on sterile 96-well flat-bottom tissue culture plates (VWR). Growth media without any cells was included as a control. Cells were grown for at least 24 hours to allow proper adherence to the growth surface. Afterwards, ADEP analogs were serially diluted and introduced to the tissue cultures via fresh growth media at 50 μL per well. Inclusion of activators / DMSO brought the final DMSO concentration of the growth media up to a maximum of 0.5% (v:v). For experiments that involve overexpression of FLAG-tagged HsClpP (WT or S153A mutant), Dox (Sigma-Aldrich) was also applied at 0.4 μg/mL (final concentration) as needed. A total of four independent replicates were prepared for each cell line and for each growth condition used. Cells were grown in the presence of ADEP / DMSO for 72 hours.

To assess cell survival, live adherent cells were fixed with 10% (w:v) trichloroacetic acid (TCA) at 4°C for 1-2 hours. The tissue culture plates were then rinsed with water to remove dead cells and cell debris and air-dried overnight. Fixed cells were stained with a solution of 0.4% (w:v) sulforhodamine B (SRB) (Sigma-Aldrich) dissolved in 1% (v:v) acetic acid at room temperature for 30 minutes, followed by plate-rinsing with 1% acetic acid and air-drying. The SRB retained was extracted with 10 mM of Tris base (200 μL per sample). Absorbance at λ = 510 nm (A_{510}) was then measured using the EnSpire 2300 Multilabel Reader. A_{510} is linearly proportional to the amount of cellular protein present in each sample.

To determine the IC_{50} for the ADEP analogs, relative cell viability (RCV) values were calculated by normalizing the A_{510} readings in ADEP-containing sample to the DMSO-only control. Plots of RCV vs. ADEP concentration were constructed, followed by non-linear regression analysis using a standard dose response equation, to determine the required IC_{50} values.

$$RCV = RCV_{min} + \frac{RCV_{max} - RCV_{min}}{1 + 10^{(\log IC_{50} - \log[\mathrm{ADEP}])h}}$$

In this equation, RCV_{min} and RCV_{max} are the minimum and maximum RCV observed, respectively; [ADEP] is the molar concentration of ADEP applied; and *h* is the Hill coefficient. For HEK293 T-REx *CLPP*$^{-/-}$ and HEK293 T-REx *CLPP*$^{-/-}$ *ΔCLPX** cells, IC_{50} values were estimated by manual examination of the plotted data due to the lack of a minimum plateaus, which prohibited meaningful analysis using the Hill model.

Mitochondrial Proteome Profiling for WT and *CLPP*$^{-/-}$

HEK293 T-REx WT and *CLPP*$^{-/-}$ cells were grown to ~80% confluence, with two biological replicates prepared for WT and three for *CLPP*$^{-/-}$. All cells were chemically crosslinked by treatment with 0.5 mM of the cell membrane-permeable crosslinker dithiobis succinimidyl propionate (DSP) for 30 min at room temperature. The crosslinking reagent was quenched from the samples by the addition and incubation with 100 mM Tris-HCl (pH 7.5) and 2 mM EDTA for 10 min at room temperature. Cells were suspended by gentle pipetting and harvested by centrifugation at 600 x g for 5 min and then washed twice in ice-cold NKM buffer [10 mM TrisHCl pH 7.5, 130 mM NaCl, 5 mM KCl, and 7.5 mM $MgCl_2$]. The pellet was resuspended in ice-cold buffer containing 10 mM TrisHCl (pH 6.8), 130 mM NaCl, 10 mM KCl, 150 mM $MgCl_2$, 1 mM PMSF, and 1 mM DTT. The resuspended cells were then allowed

to swell for 10 min, followed by lysis via repeated passages through a syringe fitted with a 23-gauge needle. Cell lysates were added to 1 cell-pellet-volume of 2 M sucrose and centrifuged at 1300 x g for 5 min at 4°C. The resulting supernatant was further centrifuged at 7,000 x g for 10 min at 4°C to pellet the mitochondrial fraction.

To lyse the mitochondrial fraction and further alkylate the mitochondrial proteins, the pellet was dissolved in 8 M urea, 20 mM TrisHCl pH 7.5 and 8 mM chloroacetamide, and subjected to sonication for 30 s with 15-30 s cooling cycles for 3 min on ice. After incubating the lysate at room temperature for 30 min, 50 mM TrisHCl was added to dilute the urea concentration from 8 M to 2 M. To this mixture, 20 mM DTT and 5 μg/mg-of-sample of Trypsin Gold (Promega) were also added to trypsinize the proteins overnight at room temperature. Trypsin activity was stopped by adding 1 μL of trifluoroacetic acid until a pH of 2-3 was reached. After desalting the samples using the C18 packed tips (Glygen Corp), the bound peptides were eluted for the tips with 0.1% formic acid and 60% acetonitrile. Protein content for WT and *CLPP*$^{-/-}$ samples was assessed by Bradford assay and adjusted to 0.9 mg. These were then dried and resuspended in 1 % formic acid for mass spectrometry analysis.

All samples were analyzed by a Proxeon EASY nanoLC 1000 System (Thermo-Fisher Scientific) coupled to an Orbitrap Elite mass spectrometer (Thermo-Fisher Scientific). For chromatographic separation, 5 μL of WT and *CLPP*$^{-/-}$ samples with same protein concentration was loaded onto an Acclaim PepMap C18 column (15 cm x 50 μm ID, 3 μm, 100 Å; Thermo-Fisher Scientific). Peptides were separated using the following elution gradients at time points in sequence: 0-3% B (0-2 min); 3-24% B (2-170 min); 24-100% B (172-190 min); 100% B (190-200 min). For this step, Buffer A refers to 0.1 % formic acid and Buffer B refers to 0.1 % formic acid in acetonitrile. Separation of peptides was achieved at a column flow rate of 0.30 μL/min. Eluted peptides were immediately ionized by positive electrospray ionization at an ion source temperature of 250°C and an ion spray voltage of 2.1 kV. Full-scan MS spectra (m/z 350–2000) was acquired in the Orbitrap at mass resolution of 60000 (m/z 400) using the positive ion mode. The automatic gain control was set at 1e6 for full FTMS scans and 5e4 for MS/MS scans. Fragmentation was performed with collision-induced dissociation (CID) in the linear ion trap with an ion intensity of > 1500 counts. The 15 most intense ions isolated for ion trap CID with charge states $\geq$ 2 were sequentially fragmented using the normalized collision energy setting at 35 %, activation Q at 0.250, and an activation time of 10 ms. Ions selected for MS/MS were dynamically excluded for 30 s.

The mass spectra files were then searched using MaxQuant ver. 1.6.1.0 (Max Planck Institute) against a UniProt human protein database of canonical sequences. The resulting data were filtered for contaminants and reverse matches. The protein intensities of the detected mitochondrial proteins were normalized against the pooled WT samples, and Student *t*-test was used to identify proteins with a 1.5-fold change (*CLPP*$^{-/-}$ / WT) at a *p*-value significance $\leq$ 0.05.

Light and Fluorescence Microscopy

HEK293 T-REx WT and *CLPP*$^{-/-}$ cells were grown on glass cover slips placed in a 6-well tissue culture plate. Prior to use, the cover slips were cleaned by treatment with 1 M HCl for 2-3 days, followed by thorough rinsing with distilled water and a second treatment with 95% ethanol for 16-18 hours. The cleaned cover slips were sterilized by autoclaving and dried under UV light. To ensure proper attachment of the cells, the sterilized cover slips were coated with gelatin by application of a 0.2% solution and incubation at 37°C for at least 2 hours. Excess gelatin solution was then removed, and the cover slips were allowed to dry in a sterile environment for 2-4 hours before use.

WT cells treated with ADEP-41 were seeded at a density of 1 x 10^5 cells/mL (2 mL per well) to compensate for lack of cell growth and division resulting from the ADEP treatment. WT cells treated with DMSO and *CLPP*$^{-/-}$ cells treated with ADEP-41 or DMSO were all seeded at 5 x 10^4 cells/mL (2 mL per well). After the cells have adhered properly, ADEP-41 (20 μM for a 24-hour treatment; 10 μM for a 72-hour treatment) or DMSO was applied via media exchange (final DMSO concentration at 0.2% for all samples). Cells were then grown for 24 or 72 hours prior to fixing and permeabilization for microscopy.

Cells were fixed in the presence of 4% formaldehyde at room temperature for 30-45 minutes, followed by membrane permeabilization with 0.1% Triton X-100 (in PBS from Gibco) supplemented with 0.1% sodium citrate at room temperature for 30 minutes. All samples were rinsed gently with PBS in between steps. For the TUNEL (Terminal deoxynucleotidyl transferase dUTP nick end labelling) assay, the fixed and permeabilized cells were labelled using the *In Situ* Cell Death Detection Kit, Fluorescein (Roche-11684795910), following the manufacturer's instructions. Cells were mounted onto standard glass microscope slides with DAPI Fluoromount-G (Southern Biotech) for visual examination using the Eclipse 80i fluorescence microscope (Nikon) equipped with the X-Cite Series 120Q excitation light source (Excelitas Technologies). Both light and fluorescence microscopic images were captured and analyzed using the NIS-Elements Basic Research Software (Nikon).

3D Structured Illumination Microscopy (3DSIM)

HEK293 T-REx WT and *CLPP*$^{-/-}$ cells were seeded on coverslips (Electron Microscopy Sciences) pre-coated with poly-D-lysine hydrobromide (Sigma-Aldrich) in a 12-well culture plate (Falcon). Cells were grown for 24 hours to allow adhesion, followed by treatment with 2 μM ADEP-41 or DMSO in the same manner as described in previous sections, for 24 or 72 hours. At these time points, the original media was removed, and cells were incubated for 30 minutes at 37°C, 5% CO_2 with 200 nM MitoTracker Red CMXRos (Molecular Probes) in Opti-MEM™ Reduced Serum Medium (Gibco). Cells were then washed once with PBS and fixed with 4% (v/v) paraformaldehyde (Electron Microscopy Sciences) in PBS for 20 minutes at room temperature. The fixed cells were then washed twice with PBS, permeabilized with 0.2% (v/v) Triton X-100 (BioShop) in PBS for 10 minutes at room temperature and incubated with 2 μg/ml Hoechst 33342 (Molecular Probes) in PBS for 10 minutes at room temperature to counterstain nuclei.

Coverslips were then washed three times with PBS + 0.05% (v/v) Tween-20 and mounted on microscope glass slides (VWR) using 0.5% (w/v) propyl gallate (Sigma-Aldrich) dissolved in glycerol as the mounting medium.

3DSIM data were collected on the ELYRA PS.1 super resolution microscope (Carl Zeiss Microscopy) using a 63X (1.4 NA) Plan-Apochromatic oil immersion objective (Carl Zeiss Microscopy) and a 1.6X Optovar. For imaging, fluorophores were laser-excited at wavelengths 405 nm and 555 nm, and the emissions were collected with band-pass 420-480, 570-620 filters, respectively. Z-stacks were acquired over a 10-μm thickness with 101 nanometre-steps, using an iXon 885 EMCCD camera (Andor). For each image field, grid excitation patterns were acquired for five phases and three rotation angles (-75°, -15°, +45°). Raw data were reconstructed using the SIM module of ZEN Black software version 8.1 (Carl Zeiss Microscopy), with a Wiener noise filter value of -5. The final images were obtained from the reconstructed data by using a maximum intensity projection (MIP) algorithm, implemented by the ZEN Black software.

Western Blots

HEK293 T-REx WT, HEK293 T-REx *CLPP*$^{-/-}$, HeLa (regular), HeLa T-REx, U2OS and undifferentiated SH-SY5Y cells were grown in the presence of ADEP or DMSO as described in previous sections. Cells were harvested by the standard trypsinization protocol and counted with a hemocytometer. Cell lysates were prepared by first re-suspending the cells in PBS at 5 x 10^6 cells/mL, followed by sonication. Proteins in the lysates were analyzed by Western blotting using Immobilin-P PVDF membranes (EMD Millipore). Blots were imaged and analyzed with the ChemiDoc XRS+ System (BioRad). Quantification of HsClpP expression was performed by densitometry using the Quantity One 1D Analysis Software (BioRad). HsClpP expression levels were corrected for sample loading errors and normalized to the expression level in HEK293 T-REx WT. Primary antibodies for HsClpP, HsClpX and GAPDH were purchased from Abcam. Primary antibodies for Caspase-8, Caspase-9 and PUMA were purchased from Cell Signaling Technologies. The primary antibody for Caspase-3 was purchased from R&D Systems. Primary antibodies for Mcl-1 and Bcl-2 were purchased from EMD Millipore. The primary antibody for the FLAG-tag was purchased from Sigma-Aldrich. HRP-conjugated goat anti-rabbit IgG (for HsClpX, Caspase-8, Caspase-9 and PUMA) and HRP-conjugated goat anti-mouse IgG (for HsClpP, Mcl-1, Bcl-2, GAPDH and FLAG-tag) were purchased from BioRad. HRP-conjugated rabbit anti-goat IgG (for Caspase-3) was purchased from Sigma-Aldrich.

Cellular Respiration Analysis

HEK293 T-REx WT and *CLPP*$^{-/-}$ cells were seeded onto Seahorse XF96 Cell Culture Microplates (Agilent) pre-coated with poly-D-lysine (Sigma-Aldrich). Adherent cells were then grown for 24 hours in the presence of 1 μM of ADEP-41 or DMSO as described in previous sections. Cellular respiration was assessed using the Seahorse XF Cell Mitochondrial Stress Kit (Agilent) following the manufacturer's protocol. Oxygen consumption rate (OCR) and extracellular acidification rate (ECAR) were monitored using the Seahorse XFe96 Analyzer (Agilent) fitted the XFe96 sensor cartridge (Agilent). Carbonyl cyanide-*4*-(trifluoromethoxy)phenylhydrazone (FCCP) that was included in the Mitochondrial Stress Kit was applied to the cell cultures at a final concentration of 0.25 μM. Application of other reagents were done as outlined in the manufacturer's experimental guidelines. Data analysis was performed with the Wave Desktop program (Agilent) following the manufacturer's instructions. For OCR and ECAR normalization, cells were first fixed with 4% formaldehyde as described in previous sections. Nuclear DNA of the fixed cells was stained with Hoechst 33342 (Invitrogen) dissolved in PBS at 5 μg/mL for 30 minutes at room temperature, followed by three rounds of washes with PBS. To measure Hoechst 33342 fluorescence, 50 μL of PBS was applied to each well, followed by fluorescence measurements (λ_{ex} = 350 nm; λ_{em} = 461 nm) using the EnSpire 2300 Multilabel Reader. Fluorescence data were expressed arbitrarily in 10^4 HFU (Hoechst fluorescence units) to keep the normalized OCR and ECAR within conventional numerical ranges. Operation of the Seahorse XFe96 Analyzer and data collection was performed by the SPARC BioCentre (Hospital for Sick Children, Toronto, Canada).

QUANTIFICATION AND STATISTICAL ANALYSIS

Statistical analyses and software that were used for specific experiments have been described in the relevant subsections under Method Details. Additional statistical parameters, such as standard deviations (SD) of quantitative data, are explained in the corresponding figure legends. In general, all quantitative data were collected from at least three independent replicates and are presented as means ± SD. All enzyme kinetics experiments and cytotoxicity assays on mammalian cells were repeated multiple times to ensure data reproducibility. Quantitative microscopy data for TUNEL were derived from examining at least 50 cells per sample replicate per repeated experiment.

DATA AND SOFTWARE AVAILABILITY

The structure of the ADEP-28-HsClpP complex has been deposited in the Protein Data Bank (PDB) under the accession number 6BBA. All software used for the experiments presented here are available at the sources listed in the Key Resources Table.

SUPPLEMENTAL ITEMS

Acyldepsipeptide analogs dysregulate human mitochondrial ClpP protease activity and cause apoptotic cell death

Keith S. Wong[1], Mark F. Mabanglo[1], Thiago V. Seraphim[1,2], Antonio Mollica[1,3], Yu-Qian Mao[1], Kamran Rizzolo[1], Elisa Leung[1], Mohamed T. Moutaoufik[2], Larissa Hoell[2], Sadhna Phanse[2], Jordan Goodreid[4], Leandro R. S. Barbosa[5], Carlos H. I. Ramos[6], Mohan Babu[2], Vito Mennella[1,3], Robert A. Batey[4], Aaron D. Schimmer[7], Walid A. Houry[1,4,†]

[1]Department of Biochemistry, University of Toronto, Toronto, Ontario M5G 1M1, Canada

[2]Department of Biochemistry, University of Regina, Regina, Saskatchewan S4S 0A2, Canada

[3]Cell Biology Program, The Hospital for Sick Children, Toronto, Ontario M5G 0A4, Canada

[4]Department of Chemistry, University of Toronto, Toronto, Ontario M5S 3H6, Canada

[5]Institute of Physics, University of São Paulo, São Paulo SP, 05508-090 Brazil

[6]Institute of Chemistry, University of Campinas UNICAMP, Campinas SP, 13083-970 Brazil

[7]Princess Margaret Cancer Centre, University Health Network, Toronto, Ontario M5G 2M9, Canada

[†]Corresponding author and lead contact

Address: Department of Biochemistry, University of Toronto, 661 University Avenue, MaRS Centre, West Tower, Room 1612, Toronto, Ontario M5G 1M1, Canada.

Phone (416) 946-7141

FAX (416) 978-8548

Email walid.houry@utoronto.ca

LEGENDS FOR SUPPLEMENTAL FIGURES

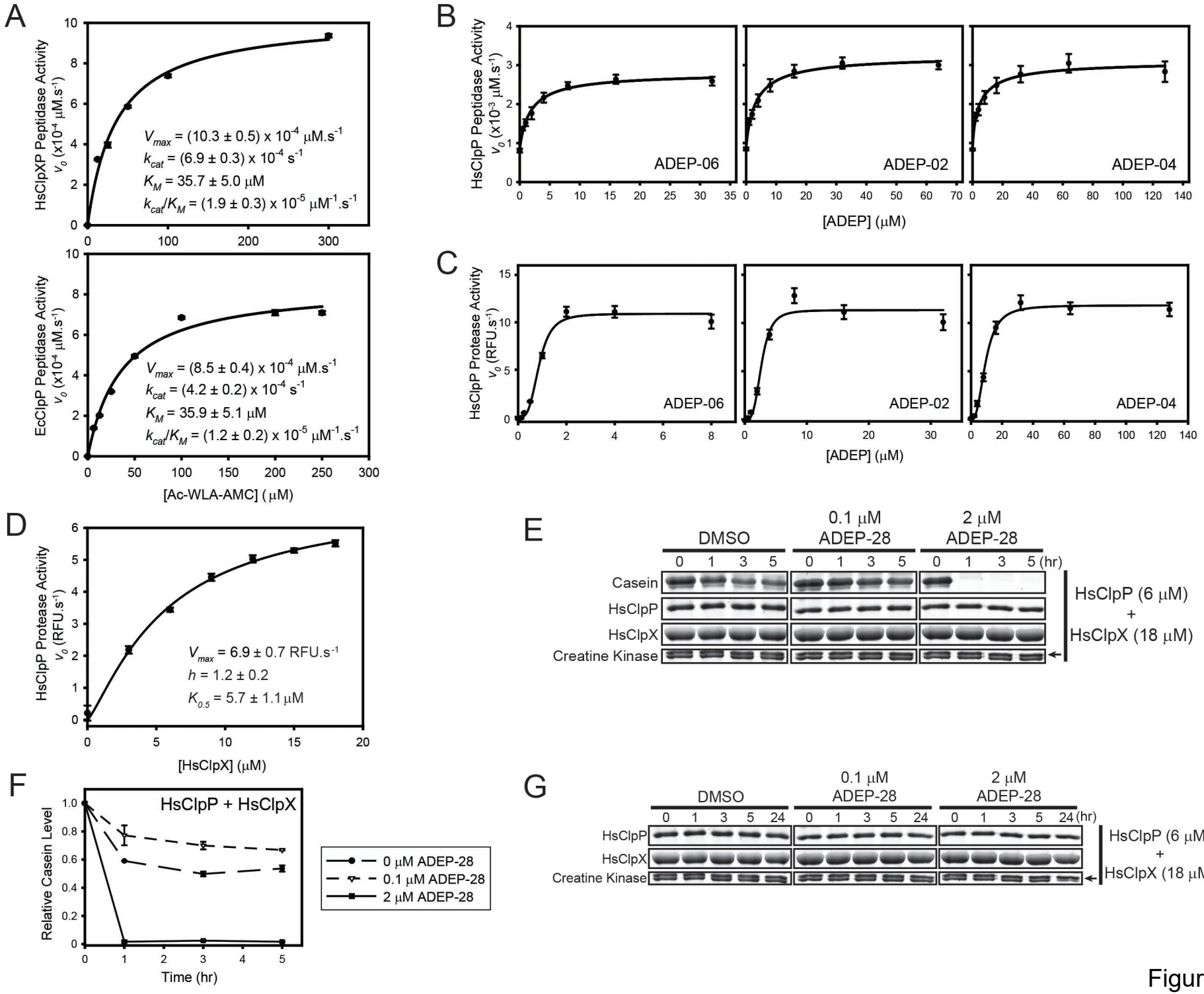
A
HsClpXP Peptidase Activity
v_0 (x10^{-4} μM.s^{-1})
V_{max} = (10.3 ± 0.5) x 10^{-4} μM.s^{-1}
k_{cat} = (6.9 ± 0.3) x 10^{-4} s^{-1}
K_M = 35.7 ± 5.0 μM
k_{cat}/K_M = (1.9 ± 0.3) x 10^{-5} μM^{-1}.s^{-1}
EcClpP Peptidase Activity
v_0 (x10^{-4} μM.s^{-1})
V_{max} = (8.5 ± 0.4) x 10^{-4} μM.s^{-1}
k_{cat} = (4.2 ± 0.2) x 10^{-4} s^{-1}
K_M = 35.9 ± 5.1 μM
k_{cat}/K_M = (1.2 ± 0.2) x 10^{-5} μM^{-1}.s^{-1}
[Ac-WLA-AMC] (μM)
B
HsClpP Peptidase Activity
v_0 (x10^{-3} μM.s^{-1})
ADEP-06
ADEP-02
ADEP-04
[ADEP] (μM)
C
HsClpP Protease Activity
v_0 (RFU.s^{-1})
ADEP-06
ADEP-02
ADEP-04
[ADEP] (μM)
D
HsClpP Protease Activity
v_0 (RFU.s^{-1})
V_{max} = 6.9 ± 0.7 RFU.s^{-1}
h = 1.2 ± 0.2
$K_{0.5}$ = 5.7 ± 1.1 μM
[HsClpX] (μM)
E
DMSO
0.1 μM ADEP-28
2 μM ADEP-28
0 1 3 5 0 1 3 5 0 1 3 5 (hr)
Casein
HsClpP
HsClpX
Creatine Kinase
HsClpP (6 μM) + HsClpX (18 μM)
F
HsClpP + HsClpX
Relative Casein Level
Time (hr)
0 μM ADEP-28
0.1 μM ADEP-28
2 μM ADEP-28
G
DMSO
0.1 μM ADEP-28
2 μM ADEP-28
0 1 3 5 24 0 1 3 5 24 0 1 3 5 24 (hr)
HsClpP
HsClpX
Creatine Kinase
HsClpP (6 μM) + HsClpX (18 μM)

Figure S1

Figure S1. Related to Figure 2. Enhancement of peptidase and protease activity of HsClpP by ADEP-06, ADEP-02 and ADEP-04.

(A) Michaelis-Menten kinetic analysis of Ac-WLA-AMC cleavage by 1.5 μM HsClpP in the presence of 4.5 μM HsClpX (upper panel) and by 2 μM EcClpP (lower panel). In both experiments, the kinetic parameters shown were derived from non-linear regression analysis of the initial rates. Error bars shown correspond to standard deviations (SDs) derived from at least three independent replicates. Statistical errors shown for the calculated kinetic parameters correspond to curve-fitting errors.

(B) Enhancement of the peptidase activity of HsClpP by ADEP-06, ADEP-02 and ADEP-04. The kinetic data shown in each panel were derived from three independent replicates.

(C) Enhancement of the protease activity of HsClpP by ADEP-06, ADEP-02 or ADEP-04. The kinetic data shown in each panel were derived from three independent replicates.

(D) Kinetic analysis of the degradation of casein-FITC by HsClpP in the presence of HsClpX at different molar ratios. Data points were analyzed by non-linear regression using the Hill equation. Relevant kinetic parameters derived from the analysis are as shown.

(E) Degradation of unlabelled casein by HsClpX and HsClpP in the absence (DMSO panels) and presence of ADEP-28 at 0.1 μM (middle panels) and 2 μM (right panels), observed on SDS-PAGE gels. The arrow to the right of creatine kinase panels indicates the correct band for creatine kinase.

(F) Densitometry analysis of casein degradation from (D). Data points were derived from 3 independent replicates.

(G) Levels of HsClpX and HsClpP in the reaction observed by SDS-PAGE over 24 hours. The arrow to the right of creatine kinase panels indicates the correct band for creatine kinase.

A

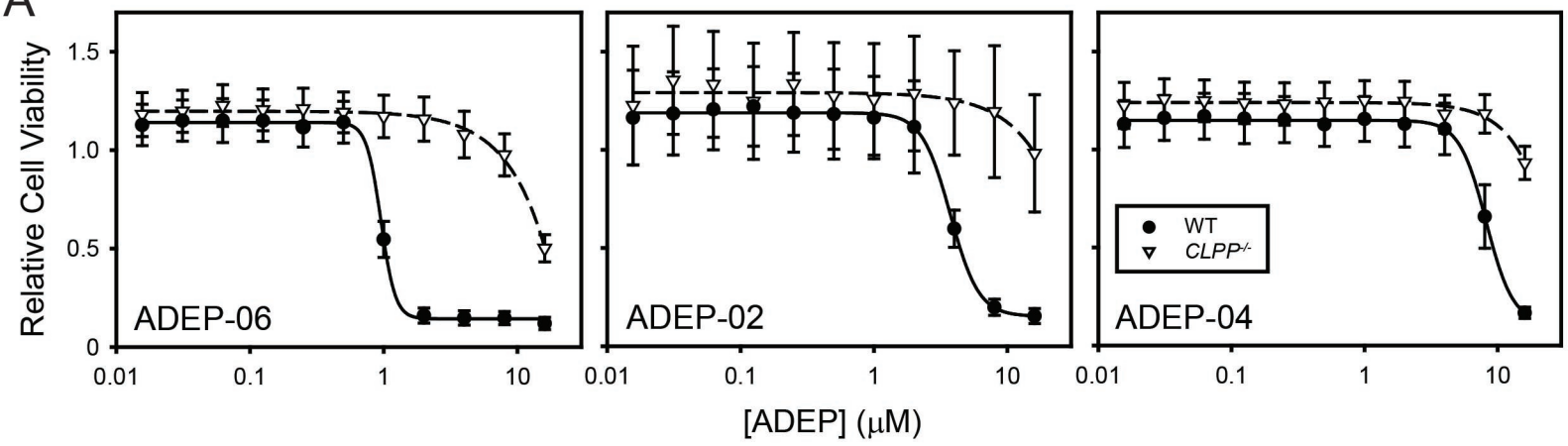

B

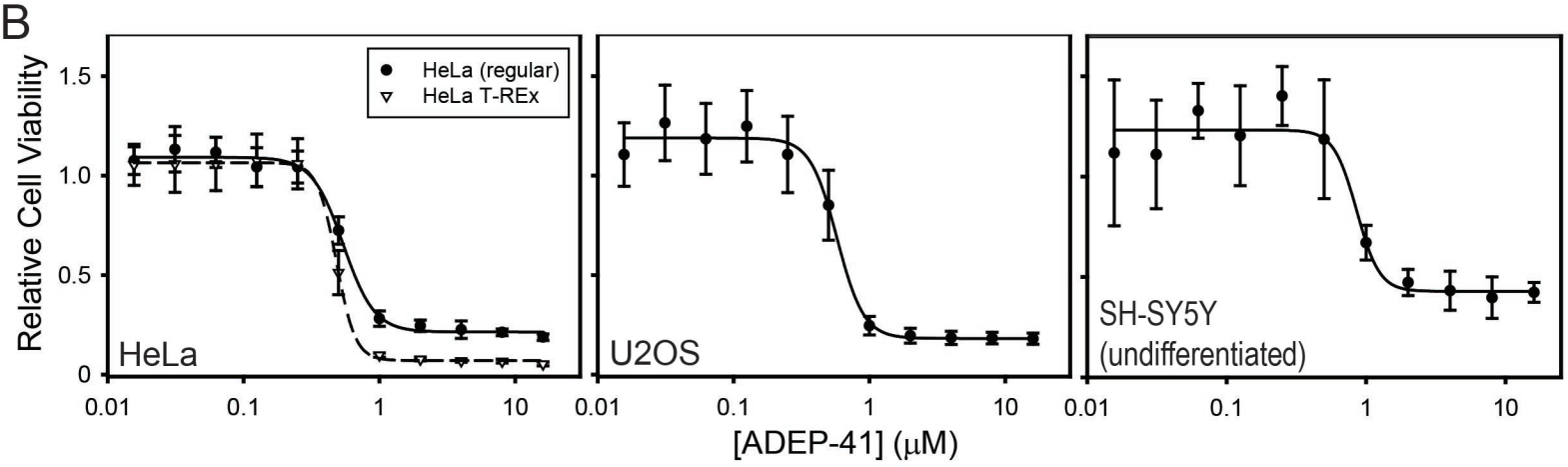

C

	IC_{50} with ADEP-41 (μM)
HEK293 T-REx WT	0.49 ± 0.02
HeLa (regular)	0.54 ± 0.02
HeLa T-REx	0.48 ± 0.01
U2OS	0.58 ± 0.03
SH-SY5Y (undifferentiated)	0.86 ± 0.12

D

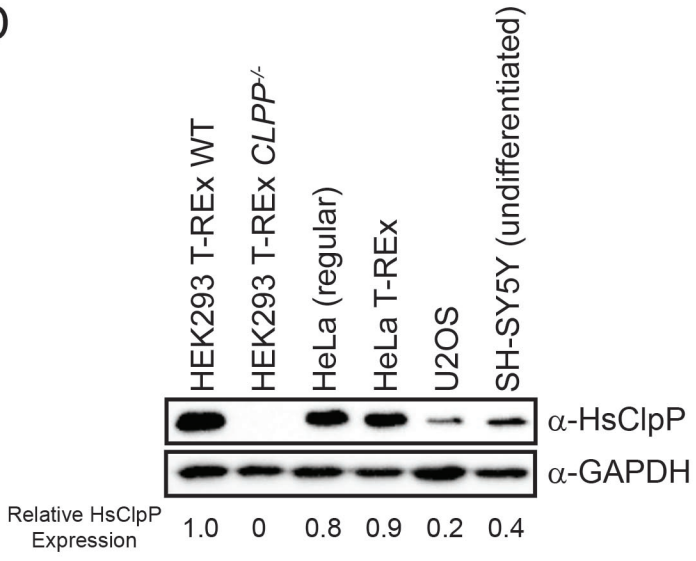

Figure S2

Figure S2. Related to Figure 3. ADEP-induced cytotoxicity is partially dependent on cell type.

(A) Cytotoxicity profiles of HEK293 T-REx WT (*CLPP*$^{+/+}$) and HEK293 T-REx *CLPP*$^{-/-}$ cells treated with ADEP-06 (left panel), ADEP-02 (middle panel) and ADEP-04 (right panel). The relative cell viability was calculated by normalizing all data points to the DMSO-only control for each data set. Data points were collected from 4 independent replicates.

(B) ADEP-41 cytotoxicity profiles of HeLa (regular) and HeLa T-REx (left panel), U2OS (middle panel) and undifferentiated SH-SY5Y cells (right panel). Relative cell viability was calculated by normalizing all data points to the DMSO-only control for each data set. Data points were collected from 4 independent replicates.

(C) IC_{50} derived from the cytotoxicity profiles shown in (B) by non-linear regression analysis using the standard dose response equation (see Methods). The IC_{50} for HEK293 T-REx WT is identical to the one shown in Figure 3B.

(D) Western blot for endogenous HsClpP expression in HEK 293 T-REx WT, HEK 293 T-REx *CLPP*$^{-/-}$, HeLa (regular), HeLa T-REx, U2OS, and undifferentiated SH-SY5Y. GAPDH is used as the loading control. The numbers at the bottom represent intracellular HsClpP level in each cell line, relative to HEK293 T-REx WT.

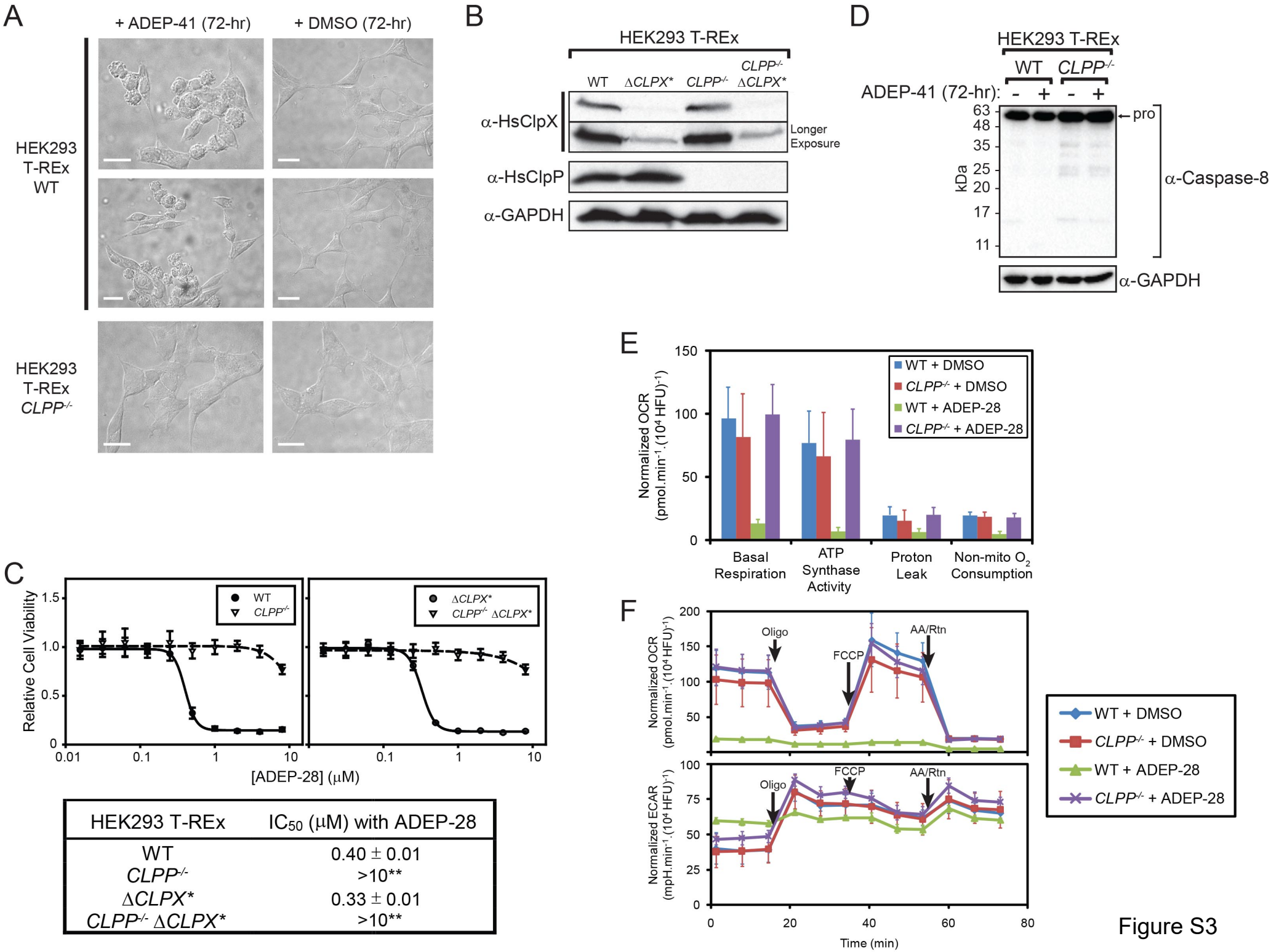

HEK293 T-REx	IC_{50} (μM) with ADEP-28
WT	0.40 ± 0.01
CLPP$^{-/-}$	>10**
Δ*CLPX**	0.33 ± 0.01
CLPP$^{-/-}$ Δ*CLPX**	>10**

Figure S3

Figure S3. Related to Figure 4. Supporting evidence for the activation of the intrinsic, caspase-dependent apoptosis in ADEP-induced cytotoxicity.

(A) Light microscopy on HEK293 T-REx WT (top 2 rows) and HEK293 T-REx *CLPP*$^{-/-}$ cells (bottom row) treated with 10 μM of ADEP-41 (panels on left column) or DMSO (panels on right column) over 72 hours. The white bars shown are 100 μm.

(B) Western blot for HsClpX, HsClpP and GAPDH on whole cell lysates of WT, *ΔCLPX**, *CLPP*$^{-/-}$ and *CLPP*$^{-/-}$ *ΔCLPX** cells. The blot for HsClpX is shown with normal exposure time (upper panel of α-HsClpX) and long exposure time (lower panel of α-HsClpX). GAPDH is used as the loading control.

(C) Cytotoxicity profiles of HEK293 T-REx WT and *CLPP*$^{-/-}$ cells (upper left panel) and of *ΔCLPX** and *CLPP*$^{-/-}$ *ΔCLPX** cells (upper right panel) treated with ADEP-28. The IC_{50} values are shown in the table below. Relative cell viability was calculated by normalizing all data points to the DMSO-only control for each data set. Data points were collected from 4 independent replicates. For WT and *ΔCLPX**, IC_{50} values were derived from non-linear regression analysis using a standard dose response equation (see Methods). For *CLPP*$^{-/-}$ and *CLPP*$^{-/-}$ *ΔCLPX**, the lack of a minimum plateau in the cytotoxicity profiles prohibited the derivation of IC_{50} by non-linear regression analysis. Instead, IC_{50} values were estimated and are expressed in numerical ranges (denoted by **).

(D) Western blot for Caspase-8 on whole cell lysates of WT and *CLPP*$^{-/-}$ cells treated with 10 μM ADEP-41 for 72 hours. "pro" denotes the pro form of Caspase-8. Protein molecular weight markers are shown on the left. GAPDH is used as the loading control.

(E) Respiratory (OXPHOS) profiles of WT and *CLPP*$^{-/-}$ cells during apoptosis. Cell were treated with 1 μM of ADEP-28 or DMSO prior to metabolic measurements. Cellular oxygen consumption

rate (OCR) associated with basal respiration, ATP synthase activity, proton leak and non-mitochondrial oxygen consumption (Non-mito O_2 consumption) were calculated using normalized OCR data from at least three independent replications shown in Fig. S3F (upper panel) and are shown with ± SDs.

(F) Original OXPHOS data of WT and *CLPP*$^{-/-}$ cells after a 24-hour treatment with DMSO or ADEP-28. Injection of oligomycin (Oligo), FCCP and the mixture of antimycin A and rotenone (AA/Rtn) to each sample during the experiment was done at the specific time points as shown. Both OCR (upper panel) and ECAR (lower panel) were normalized by Hoechst 33342 nuclear stain fluorescence that reflects cell count. Errors shown correspond to the SDs of individual data sets collected from at least three independently prepared replicates.

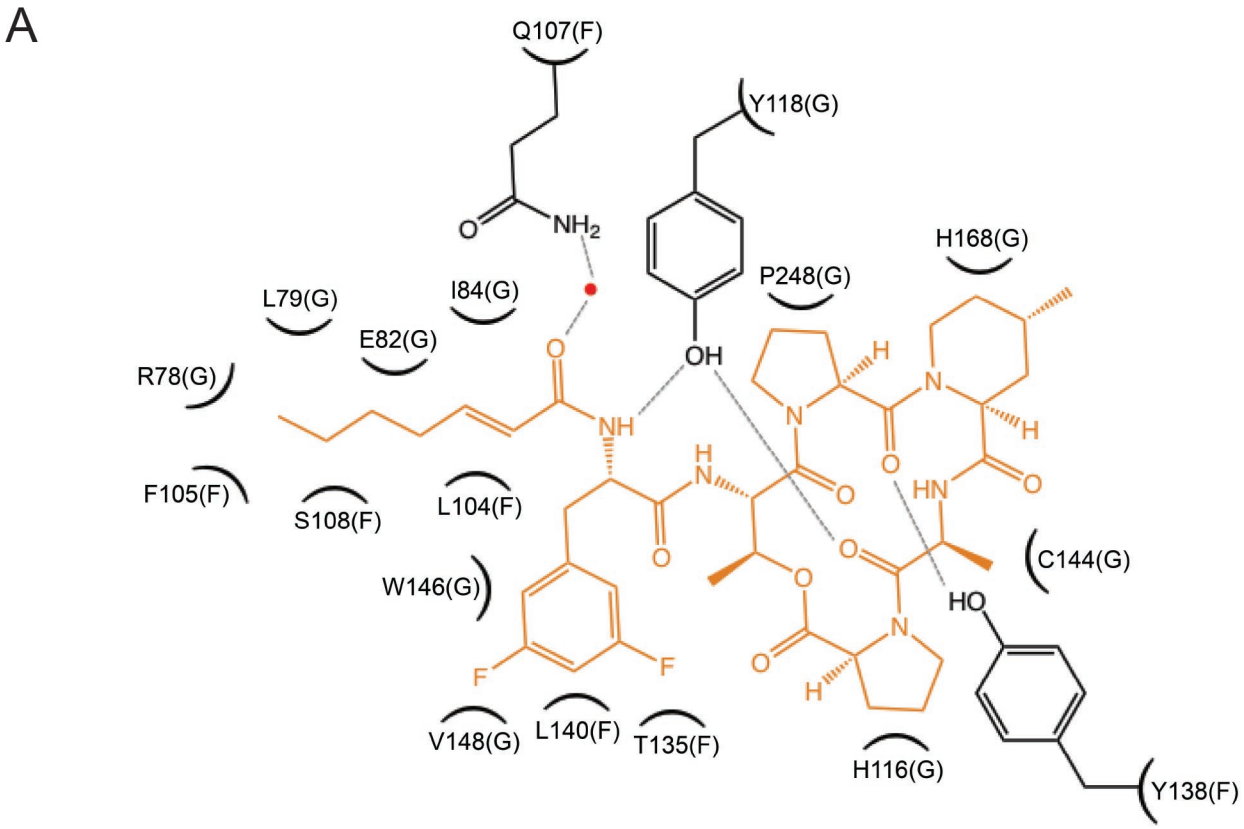
A
Q107(F)
Y118(G)
NH2
O
H168(G)
P248(G)
L79(G)
I84(G)
E82(G)
R78(G)
OH
NH
N
H
O
HN
F105(F)
S108(F)
L104(F)
W146(G)
C144(G)
HO
F
V148(G)
L140(F)
T135(F)
H116(G)
Y138(F)

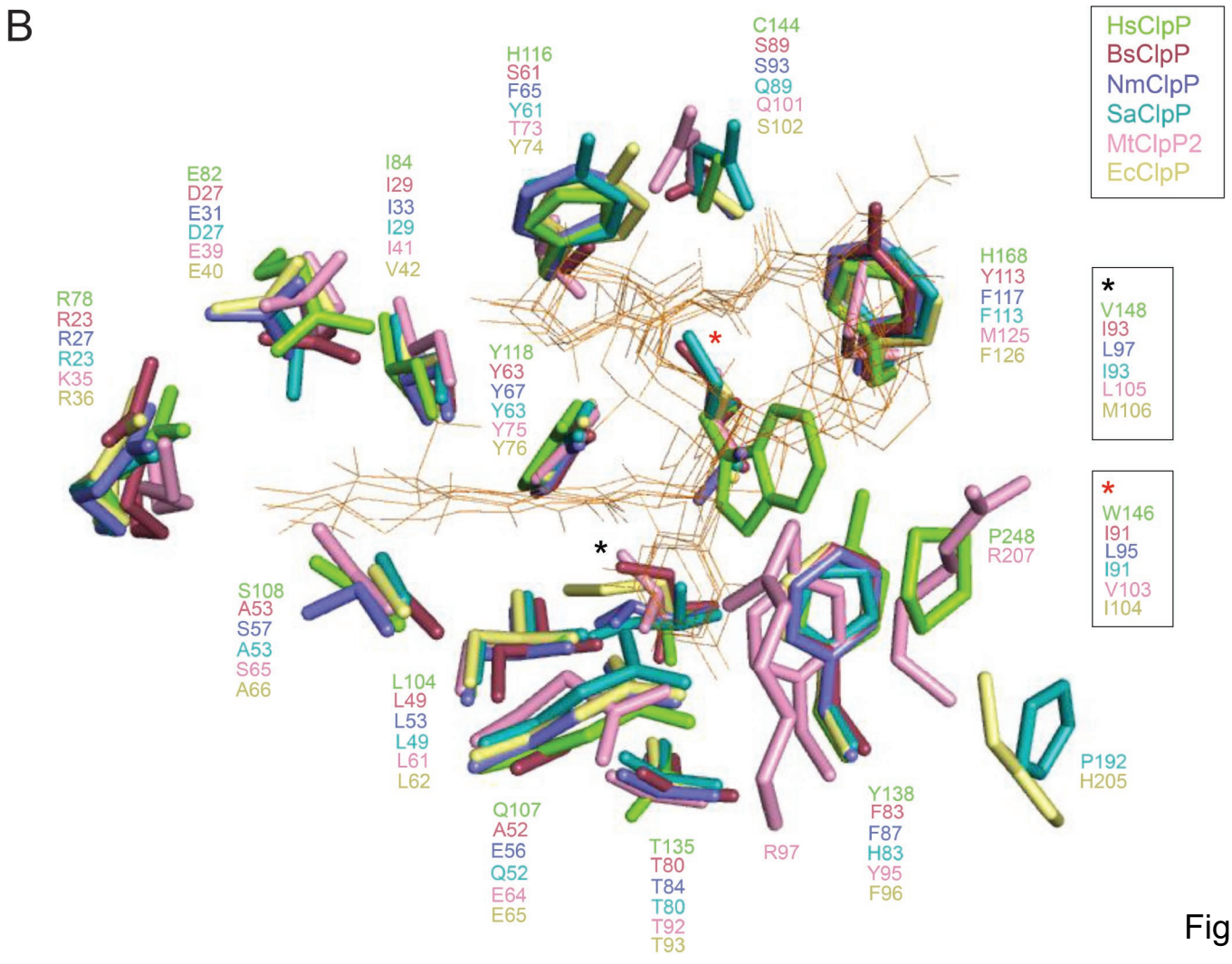
B
HsClpP
BsClpP
NmClpP
SaClpP
MtClpP2
EcClpP
C144
S89
S93
Q89
Q101
S102
H116
S61
F65
Y61
T73
Y74
E82
D27
E31
D27
E39
E40
I84
I29
I33
I29
I41
V42
H168
Y113
F117
F113
M125
F126
R78
R23
R27
R23
K35
R36
Y118
Y63
Y67
Y63
Y75
Y76
*
V148
I93
L97
I93
L105
M106
*
W146
I91
L95
I91
V103
I104
P248
R207
S108
A53
S57
A53
S65
A66
L104
L49
L53
L49
L61
L62
Q107
A52
E56
Q52
E64
E65
T135
T80
T84
T80
T92
T93
R97
Y138
F83
F87
H83
Y95
F96
P192
H205

Figure S4

Figure S4. Related to Figure to Figure 6. Structural details of the ADEP-28 binding pocket in HsClpP.

(A) A cartoon representation based on LigPlot of the ADEP-28 interactions with amino acid residues from the hydrophobic binding pocket between the two adjacent F and G subunits in HsClpP.

(B) Superposition of the amino acid residues lining the ADEP-binding pockets of ClpP from: human mitochondria (HsClpP, green; this study), *Bacillus subtilis* (BsClpP, red; PDB 3KTI (Lee et al., 2010)), *Neisseria meningitidis* (NmClpP, light blue; PDB 5DKP (Goodreid et al., 2016)), *Staphylococcus aureus* (SaClpP, teal; PDB 5VZ2 no published paper), *Mycobacterium tuberculosis* (MtClpP2, pink; PDB 4U0G (Schmitz et al., 2014)) and *Escherichia coli* (EcClpP, yellow; PDB 3MT6 (Li et al., 2010)). All amino acid residues are shown as sticks. The ADEPs are shown as very thin sticks.

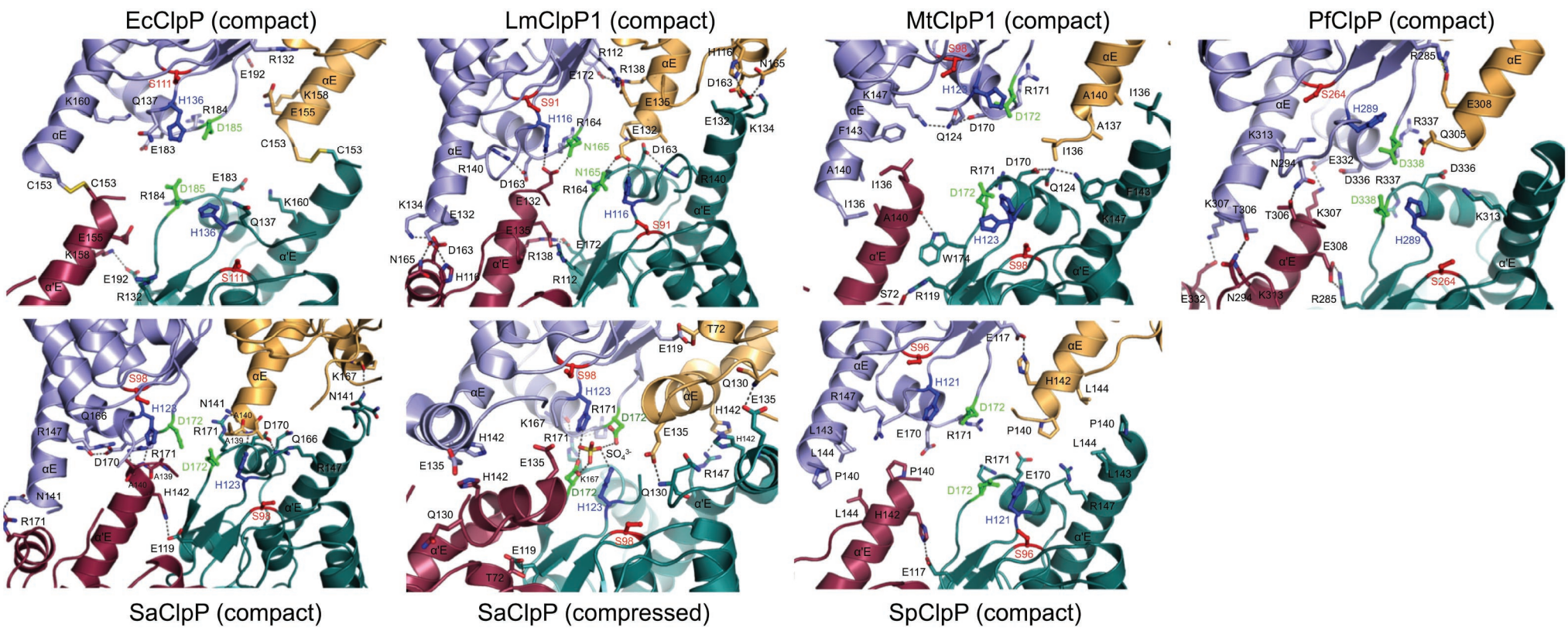
EcClpP (compact)
LmClpP1 (compact)
MtClpP1 (compact)
PfClpP (compact)
SaClpP (compact)
SaClpP (compressed)
SpClpP (compact)

Figure S5

Figure S5. Related Figures 6 and 7. Molecular interactions at the ring-ring interface of different compact and compressed ClpP structures.

The structures shown are from *E. coli* (EcClpP, 3HLN; contains a A153C mutation introducing a disulfide bridge between two apposing αE helices), *L. monocytogenes* (LmClpP1, 4JCQ), *M. tuberculosis* (MtClpP1, 2CE3), *P. falciparum* (PfClpP, 2F6I), *S. aureus* (SaClpP, 4EMM), *S. aureus* (SaClpP, 3ST9), and *S. pneumoniae* (SpClpP, 1Y7O; contains an A153P mutation). Four neighbouring subunits are represented as cartoons and coloured light blue, light orange, red, and teal, with the catalytic residues represented as ball and stick models: Ser (red), His (blue) and Asp (green).

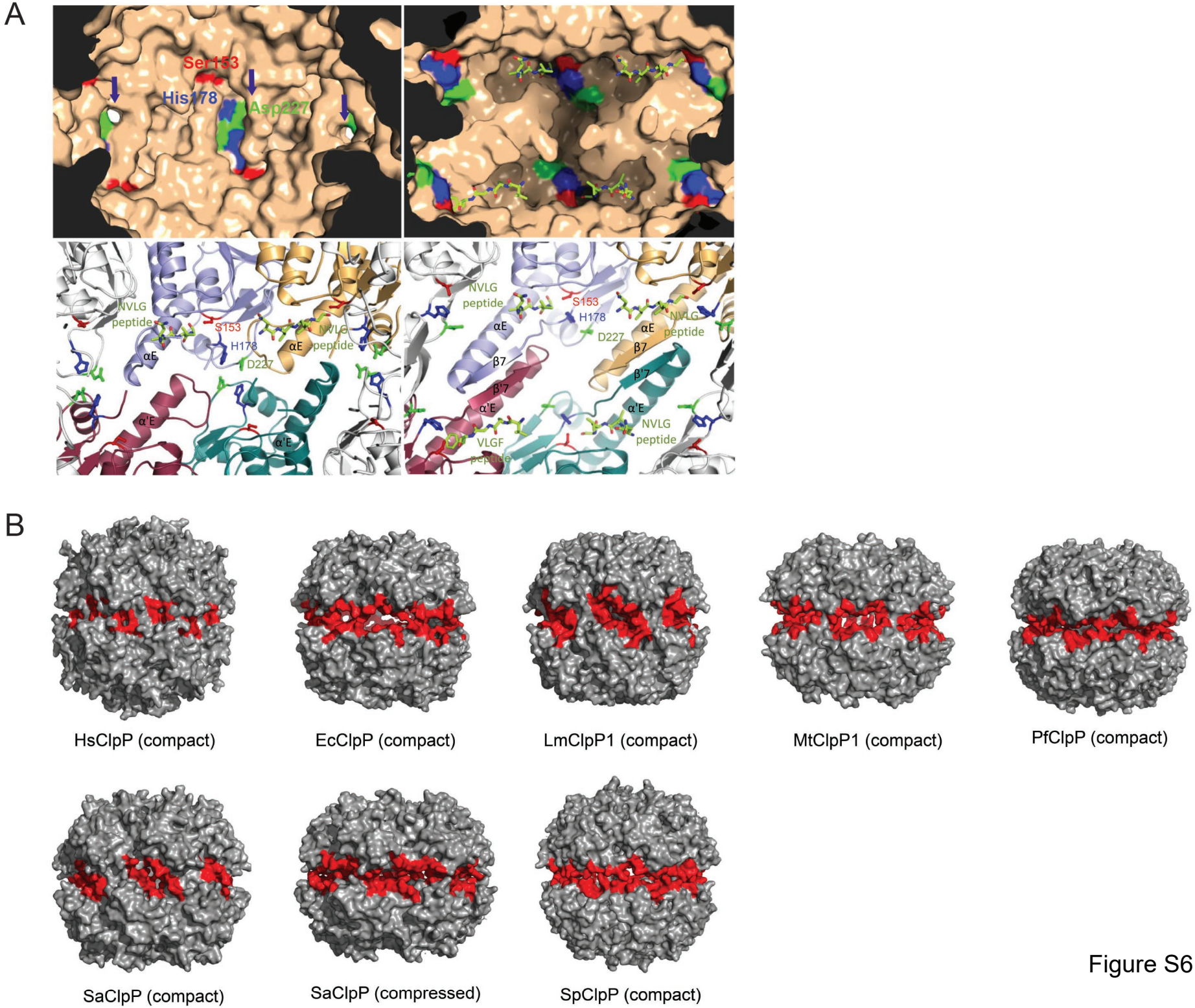
A
Ser153
His178
Asp227
NVLG peptide
S153
H178
D227
αE
α'E
β7
β'7
VLGF peptide
B
HsClpP (compact)
EcClpP (compact)
LmClpP1 (compact)
MtClpP1 (compact)
PfClpP (compact)
SaClpP (compact)
SaClpP (compressed)
SpClpP (compact)

Figure S6

Figure S6. Related to Figures 6 and 7. The presence of equatorial side pores in different ClpP structures.

(A) The structures are shown as viewed from the inside of the HsClpP tetradecamer.

Top left panel – In the compact ADEP-28-HsClpP complex, the catalytic triad is distorted such that H178 (blue surface) and D227 (green surface) form hydrogen bonding and/or electrostatic interactions with D227 and H178 residues of the apposing ring, respectively, securing the compact conformation. Distortion of the catalytic triad causes S153 to move away from H178 and D227. The side pore is located in close proximity to the catalytic site.

Top right panel – In the extended apo-HsClpP (PDB 1TG6), the active site surface is significantly different from that of the compact ADEP-28-HsClpP structure. The catalytic triads are ordered and poised for catalysis of bound peptide substrates, here shown as green sticks occupying the substrate binding cavity. The peptide substrates are shown by superimposing the structure of *H. pylori* ClpP with bound NVLGFTQ peptide (PDB 2ZL2) (Kim and Kim, 2008) to HsClpP structure.

Bottom panels – Cartoon representation of the compact ADEP-28-HsClpP complex and extended apo-HsClpP, showing the relative positions of the catalytic triads and peptide substrates. Four HsClpP subunits that form the interface are coloured light blue, light orange, red and teal, while neighbouring subunits are coloured grey. In the compact ADEP-28-HsClpP structure, the unraveling of two N-terminal turns of the αE helix forms a structured loop that impinges on the substrate binding site (bottom left panel). In contrast, in the apo-HsClpP structure, the β7 strand and αE helix are fully formed and present a cavity for substrate peptide binding.

(B) Surface representation of compact and compressed ClpP structures from human (HsClpP, this study), *E. coli* (EcClpP, PDB 3HLN), *L. monocytogenes* (LmClpP1, PDB 4JCQ), *M. tuberculosis*

(MtClpP1, PDB 2CE3), *P. falciparum* (PfClpP, PDB 2F6I), *S. aureus* (SaClpP, PDB 4EMM), *S. aureus* (SaClpP, PDB 3ST9), and *S. pneumoniae* (SpClpP, PDB 1Y7O). Equatorial side pores of distinct sizes and shapes are indicated by red surfaces that are from residues forming the rims of these pores.

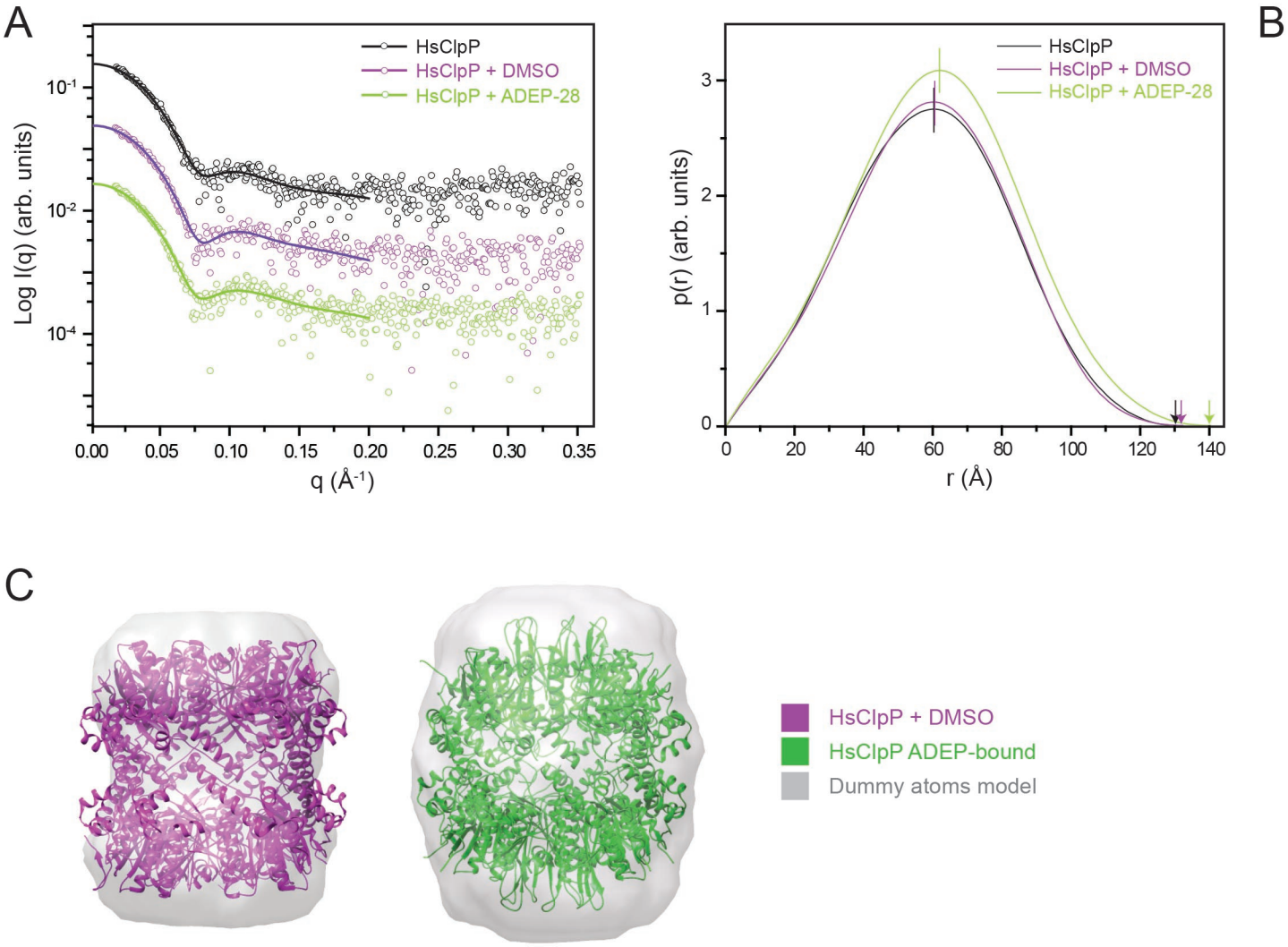
A
HsClpP
HsClpP + DMSO
HsClpP + ADEP-28
Log I(q) (arb. units)
q (Å-1)
B
p(r) (arb. units)
r (Å)
C
HsClpP + DMSO
HsClpP ADEP-bound
Dummy atoms model

Figure S7

Figure S7. Small angle X-ray scattering data for HsClpP.

(A) Scattering profiles (Log of scattering intensity as a function of the scattering vector q) of apo HsClpP in buffer, in DMSO-containing buffer and in the presence of ADEP-28. Experimental curves (open circles) were fitted using the GNOM program (solid lines). HsClpP + DMSO and HsClpP + ADEP-28 curves were divided by 10 and 100, respectively, for visualization purposes. (B) Particle distance distribution functions of HsClpP in buffer, in DMSO-containing buffer, and in the presence of ADEP-28. The vertical lines indicate maximum p(r) and arrows indicate D_{max}. (C) Shown are the X-ray structures of apo HsClpP (PDB: 1TG6) and ADEP-28-bound HsClpP superimposed on the DAMs of HsClpP + DMSO and HsClpP + ADEP-28.

SUPPLEMENTAL TABLES S3 and S4

Table S3. Related to Figures 5-7 and S4-S6. Data collection and refinement statistics of ADEP-28-HsClpP structure

Data Collection	
Space group	P 3_2 2 1
Cell dimensions	
a, b, c (Å) α, β, γ (°)	172.40, 172.40, 135.96 90.0, 90.0, 120.0,
Wavelength (Å)	1.5418
Resolution (Å)	46.73 - 2.80 (2.90 – 2.80)
R_{meas}/R_{pim}	0.188/0.056
I/σI	15.4 (1.3)
Completeness (%)	99.9 (100.0)
Redundancy	11.1 (11.0)
Refinement	
Resolution (Å)	46.73 - 2.80
No. reflections	57,813 (5,716)
R_{work}/R_{free}	0.1866/0.2346
No. atoms	10,846
Protein	10,246
Ligand	392
Water	208
B factors	
Protein	62.9
Ligand	61.3
Water	57.7
r.m.s. deviations	
Bond lengths (Å)	0.010
Bond angles (°)	1.18

Values in parentheses are for the highest resolution shell.
The highest resolution shell includes all reflections between 2.80 and 2.90 Å.
R_{work} is $\Sigma|F_o-F_c|/\Sigma F_o$.
R_{free} is the cross-validation R-factor computed for a test set of reflections (3.5% of total).

Table S4. Related to Figure S7. Size and dimension properties determined for HsClpP by SAXS

Properties	SAXS			Crystallography[6]	
	HsClpP	HsClpP + DMSO	HsClpP + ADEP-28	HsClpP	HsClpP + ADEP-28
Rg (Å)[1]	44.5	44.3	45.9	42.9	42.7
D_{max} (Å)[1]	130	132	140	136	130
$MM_{Experimental}$ (kDa)[2]	337 ± 21	344 ± 11	376 ± 21		
$MM_{Theoretical}$ (kDa)[3]	340	340	351[4]		
Oligomeric state[5]	13.9	14.2	15.1	14-mer	14-mer

[1]Properties experimentally determined using final merged SAXS curves. Rg is radius of gyration. D_{max} is maximum dimension of the molecule.
[2]$MM_{Experimental}$ is the average molecular mass determined from eleven SAXS curves.
[3]Calculated from the amino acid sequence using the Protparam program (http://web.expasy.org/protparam/).
[4]The $MM_{Theoretical}$ of compound-bound ClpP was calculated taking into account additional 14 molecules of ADEP-28 ($MM_{Theoretical}$ = 784.89 g/mol).
[5]For the SAXS data, the oligomeric state is obtained by dividing $MM_{Experimental}$ by the $MM_{Theoretical}$ of the monomer (24.2 kDa). For the crystallographic data, the oligomeric state refers to the established biological complex.
[6]Values calculated from the crystallographic structures by the program Hydropro (http://leonardo.inf.um.es/macromol/programs/hydropro/hydropro.htm).

Cell Chemical Biology
Previews

Dysregulating ClpP: From Antibiotics to Anticancer?

David A. Dougan,[1] Ingo Hantke,[2] and Kürşad Turgay[2,*]
[1]La Trobe Institute for Molecular Science, La Trobe University, Melbourne, VIC 3086, Australia
[2]Institute of Microbiology, Leibniz Universität Hannover, 30419 Hannover, Germany
*Correspondence: turgay@ifmb.uni-hannover.de
https://doi.org/10.1016/j.chembiol.2018.08.002

In this issue of *Cell Chemical Biology*, Wong et al. (2018) identify several dysregulators of a key mitochondrial protease: casein lytic protease P (ClpP). These dysregulators were found to trigger programmed cell death and may offer fresh avenues for the development of novel cancer therapeutics.

The mitochondrion is often referred to as the "powerhouse of the cell;" however, this organelle is much more than a simple factory for the production of cellular energy. The mitochondrion is also a key player in several metabolic pathways as well as a crucial component of the intrinsic apoptosis pathway. As such, the maintenance of the mitochondrial proteome in humans (from the post-translational import of these proteins to their sorting, folding, and assembly) plays a crucial role in a variety of diseases, including cancer. This process of protein homeostasis (proteostasis) within the mitochondrion is orchestrated by a conserved network of chaperones and proteases, which include the casein lytic protease (hClpP).

Similar to its bacterial counterparts, human mitochondrial hClpXP is a large protein complex composed of two components: a hexameric AAA+ (ATPase associated with a variety of cellular activities) unfoldase, hClpX, which associates with an oligomeric peptidase component, hClpP (composed of two heptameric rings, stacked back-to-back). The interaction between the two components is mediated via a tripeptide loop on hClpX (commonly referred to as the IGF loop), which docks into a hydrophobic pocket on the surface of ClpP. This interaction (between hClpX and hClpP) not only facilitates the transfer of substrates (recognized and unfolded by hClpX) into the proteolytic chamber of hClpP, but also activates the hClpP complex for the hydrolysis of these substrates into short peptides (Kang et al., 2005). Importantly, although the substrates of human mitochondrial ClpXP remain poorly defined, this protease is proposed to play a vital role in humans because it has been implicated in a variety of crucial functions from the removal of damaged and misfolded proteins (Pryde et al., 2016) to the signaling of a compartment specific unfolding protein response (UPR) known as mtUPR (Haynes and Ron, 2010). In addition, mutations in hClpP have been linked to Perrault syndrome, which in severe cases can cause ataxia or intellectual disability (Jenkinson et al., 2013).

Previously, it was known that human ClpP, like many of its bacterial relatives, is dysregulated by the novel antibiotic acyldepsipeptide (ADEP); however, neither the mode-of-action nor the physiological consequence of this activation was examined (Lowth et al., 2012). In this study, Houry and colleagues (Wong et al., 2018) have provided new insights into the mechanism of ClpP dysregulation by ADEP and demonstrate that dysregulation of mitochondrial ClpP is cytotoxic to variety of human cell types.

Using an *in vitro* screen, the authors identified several potent activators of human ClpP and characterized their effect both *in vitro* and *in vivo*. Through the use of hClpP knock out (KO) cells and cells expressing different forms of hClpP, Houry and colleagues (Wong et al., 2018) were able to demonstrate that the cytotoxic effects of ADEP *in vivo* were specifically due to the dysregulation of hClpP. The team went on to show that dysregulation of hClpP by ADEP resulted in the loss of a pro-survival protein Mcl-1, with a concomitant stabilization of the pro-apoptotic initiator PUMA, resulting in caspase activation causing cell death by the intrinsic apoptotic pathway (Figure 1). Currently, however, it remains unclear whether the cytotoxic effects of ADEP are due to the turnover of a specific mitochondrial protein or whether the wholesale loss of a range of mitochondrial proteins is required for the activation of the intrinsic pathway. Interestingly, although the molecular targets of dysregulated hClpP turnover remain unresolved at this stage, the levels of hClpX were dramatically reduced in response to ADEP addition. The turnover of hClpX, however, was not directly mediated by hClpP. So what are the targets of dysregulated hClpP? One possibility, based on our understanding of bacterial systems, is newly synthesized proteins (Kirstein et al., 2009); alternatively, newly imported proteins may be targeted by the dysregulated protease. The turnover of these potential targets would likely hinder the organelles ability to restore protein homeostasis and hence trigger apoptosis.

To better understand the mode of action of ADEP, Houry and colleagues crystallized human ClpP in complex with ADEP. Consistent with previous structures of bacterial ClpP homologs, ADEP was found to dock within the hydrophobic pocket of human ClpP, which triggered "ordering" of the N-terminal axial loops and "opening" of the axial pore (Figure 1). In addition to these expected changes, the ADEP bound structure of human ClpP was captured in a new conformation, which the authors propose represents an intermediate stage in the active cycle of ClpP. This new conformation of the hClpP-ADEP complex is more compact than previous ADEP-bound ClpP structures. The compact conformation results from significant changes at the interface of the two rings, in and around the handle region of ClpP, which causes rearrangement of the catalytic triads that places them into functionally inactive position. Although the catalytic triads are not aligned for proteolytic activity, they appear to play an important role in stabilization of the conformation, and

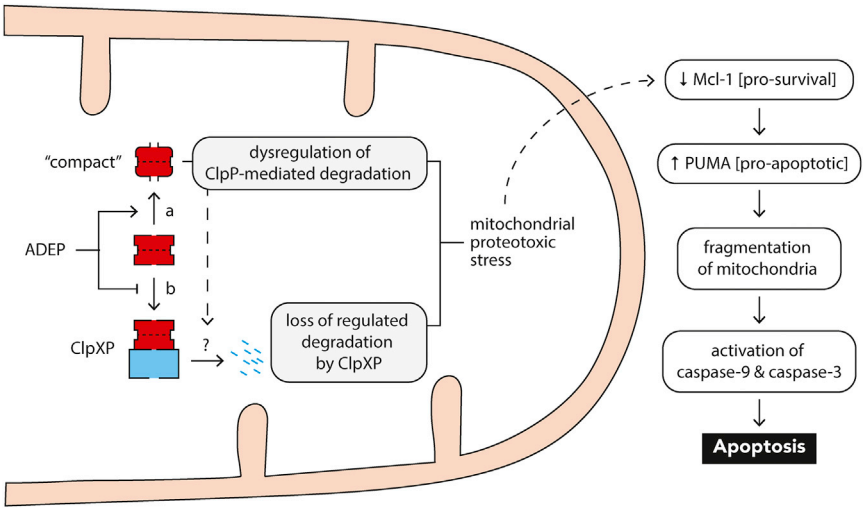

Figure 1. Addition of ADEP Dysregulates ClpP

In normal cells, mitochondrial ClpP (red), together with its partner protein ClpX (blue), is responsible for maintenance of the mitochondrial proteome. The addition of ADEP to mammalian cells results in the dysregulation of ClpP via (a) the activation of ClpX-independent degradation and (b) the inhibition of ClpX docking to ClpP, which results in the turnover of ClpX via an unknown protease. Ultimately, this results in an increase to mitochondrial proteotoxic stress and leads to a loss of the pro-survival protein Mcl-1 and an increase in the levels of the pro-apoptotic protein PUMA, followed by activation of the caspase cascade leading to apoptosis.

hence this conformation is considered an intermediate structure in the functional cycle of ClpP. In addition to rearrangement of the catalytic triads, the peptide binding site of the compact state becomes occupied and small equatorial side pores appear in close proximity to the substrate binding pocket. As such, the compact state appears to represent an inactive intermediate, which has just released the cleaved substrate from the catalytic chamber.

What is the potential of ADEP-like activators of ClpP for the treatment of cancer? Given that hClpP is overexpressed in a broad range of cancers (Seo et al., 2016), including acute myeloid leukemias (Cole et al., 2015), it is likely that many cancer cells will be more sensitive to the toxic effect of ADEP than normal cells. Although ADEPs may represent a new weapon in the growing armory required to defeat cancer, these types of compounds with their novel mode of action still have some way to go to demonstrate their potential as useful anti-cancer drugs.

Significantly, this identification of ADEPs as potent dysregulators of hClpP may pose a new challenge for the use of these types of molecules as antibiotics. Any future development of ADEP-like molecules as antibiotics will clearly have to consider interaction with human mitochondrial ClpP. Encouragingly, some ADEP variants, when tested as antibiotics, have already been shown to exhibit limited toxicity in mice or toward human cells (Brötz-Oesterhelt et al., 2005).

ACKNOWLEDGMENTS

I.H. and K.T. are supported by the Hannover School for Biomolecular Drug Research and the Deutsche Forschungsgemeinschaft. The authors declare no competing interests.

REFERENCES

Brötz-Oesterhelt, H., Beyer, D., Kroll, H.P., Endermann, R., Ladel, C., Schroeder, W., Hinzen, B., Raddatz, S., Paulsen, H., Henninger, K., et al. (2005). Dysregulation of bacterial proteolytic machinery by a new class of antibiotics. Nat. Med. *11*, 1082–1087.

Cole, A., Wang, Z., Coyaud, E., Voisin, V., Gronda, M., Jitkova, Y., Mattson, R., Hurren, R., Babovic, S., Maclean, N., et al. (2015). Inhibition of the mitochondrial protease ClpP as a therapeutic strategy for human acute myeloid leukemia. Cancer Cell *27*, 864–876.

Haynes, C.M., and Ron, D. (2010). The mitochondrial UPR - protecting organelle protein homeostasis. J. Cell Sci. *123*, 3849–3855.

Jenkinson, E.M., Rehman, A.U., Walsh, T., Clayton-Smith, J., Lee, K., Morell, R.J., Drummond, M.C., Khan, S.N., Naeem, M.A., Rauf, B., et al.; University of Washington Center for Mendelian Genomics (2013). Perrault syndrome is caused by recessive mutations in CLPP, encoding a mitochondrial ATP-dependent chambered protease. Am. J. Hum. Genet. *92*, 605–613.

Kang, S.G., Dimitrova, M.N., Ortega, J., Ginsburg, A., and Maurizi, M.R. (2005). Human mitochondrial ClpP is a stable heptamer that assembles into a tetradecamer in the presence of ClpX. J. Biol. Chem. *280*, 35424–35432.

Kirstein, J., Hoffmann, A., Lilie, H., Schmidt, R., Rübsamen-Waigmann, H., Brötz-Oesterhelt, H., Mogk, A., and Turgay, K. (2009). The antibiotic ADEP reprogrammes ClpP, switching it from a regulated to an uncontrolled protease. EMBO Mol. Med. *1*, 37–49.

Lowth, B.R., Kirstein-Miles, J., Saiyed, T., Brötz-Oesterhelt, H., Morimoto, R.I., Truscott, K.N., and Dougan, D.A. (2012). Substrate recognition and processing by a Walker B mutant of the human mitochondrial AAA+ protein CLPX. J. Struct. Biol. *179*, 193–201.

Pryde, K.R., Taanman, J.W., and Schapira, A.H. (2016). A LON-ClpP proteolytic axis degrades complex I to extinguish ROS production in depolarized mitochondria. Cell Rep. *17*, 2522–2531.

Seo, J.H., Rivadeneira, D.B., Caino, M.C., Chae, Y.C., Speicher, D.W., Tang, H.Y., Vaira, V., Bosari, S., Palleschi, A., Rampini, P., et al. (2016). The mitochondrial unfoldase-peptidase complex ClpXP controls bioenergetics stress and metastasis. PLoS Biol. *14*, e1002507.

Wong, K.S., Mabanglo, M.F., Seraphim, T.V., Mollica, A., Mao, Y.-Q., Rizzolo, K., Leung, E., Moutaoufik, M.T., Hoell, L., Phanse, S., et al. (2018). Acyldepsipeptide analogs dysregulate human mitochondrial ClpP protease activity and cause apoptotic cell death. Cell Chem. Biol. *25*, this issue, 1017–1030.

Cell
Chemical Biology
Volume 25
Number 8
August 16, 2018
www.cell.com/cell-chemical-biology